Energy-Transfer Processes in Nonstoichiometric and Stoichiometric Er^{3+}, Ho^{3+}, Nd^{3+}, Pr^{3+}, and Cr^{3+} -Codoped Ce:YAG Transparent Ceramics: Toward High-Power and Warm-White Laser Diodes and LEDs

Karol Bartosiewicz,[1,*] Agnieszka Szysiak,[2] Robert Tomala,[3] Przemysław Gołębiewski,[2] Helena Węglarz,[2] Vitali Nagirnyi,[4] Marco Kirm,[4] Ivo Romet,[4,5] Maksym Buryi,[6,7] Vitezslav Jary,[6] Romana Kucerkova,[6] Marek Wzorek,[2] and Ryszard Buczyński[2]

[1] *Faculty of Physics, Kazimierz Wielki University in Bydgoszcz, Powstancow Wielkopolskich 2, 85-090, Bydgoszcz, Poland*

[2] *Łukasiewicz Research Network - Institute of Microelectronics and Photonics, Aleja Lotników 32/46, 02-668, Warsaw, Poland*

[3] *Institute of Low Temperature and Structural Research Polish Academy of Sciences, Okólna 2, 50-422 Wrocław, Poland*

[4] *Institute of Physics, University of Tartu, W. Ostwald Str. 1, 50411, Tartu, Estonia*

[5] *Institute of Physics of Polish Academy of Sciences, Aleja Lotników 32/46, 02-668, Warsaw, Poland*

[6] *Institute of Physics of the Czech Academy of Sciences, Cukrovarnicka 10, 16200, Prague, Czech Republic*

[7] *Faculty of Nuclear Sciences and Physical Engineering, Czech Technical University in Prague, Brehova 7, 115 19 Prague, Czech Republic*

(Received 6 May 2023; revised 21 June 2023; accepted 26 June 2023; published 21 July 2023; corrected 10 April 2024)

Transparent light-converting $Y_3Al_5O_{12}$:Ce (YAG:Ce) ceramics have become promising materials for advanced light-emitting diode and laser-driven white-light-generation technology. However, their functionality is highly dependent on factors such as structural quality, uniformity of dopant distribution, the presence of defects, and the cost of fabrication. The emission of YAG:Ce ceramics remains thermally stable when high-power-density laser excitation is uniformly spread over the entire surface area of the ceramics due to light-scattering processes. The creation of light-scattering centers that can provide homogeneous white light in ceramics is crucial. One of the drawbacks of YAG:Ce as a material for converting ultraviolet emission into white light is the lack of a red component, which results in cold light and a low color rendering index. Therefore, the codoping of YAG:Ce^{3+} with red-emitting ions (Er^{3+}, Ho^{3+}, Nd^{3+}, Pr^{3+}, and Cr^{3+}) was carried out and slight nonstoichiometry was induced in the present study to improve the photoconversion parameters. The phase purity of the studied ceramics was analyzed using powder x-ray diffraction and SEM combined with energy-dispersive spectroscopy (EDS). EDS studies revealed that nonstoichiometric ceramics contained Al_2O_3 phase inclusions that acted as light-scattering centers. Optical transmittance and absorption spectra measurements revealed the presence of light-scattering centers imposed by Al_2O_3 phase inclusions and nanodefects related to perturbations of the local lattice structure by dopants. EDS mapping and photoluminescence analysis showed the formation of Ce-Ln,Cr (Cr is a transition metal) pairs and the availability of energy transfer between the pair-forming ions. Intrinsic thermal quenching of Ce^{3+} luminescence started above 400 K. The nonstoichiometric YAG:Ce, Nd sample showed luminescence stability up to 650 K with a luminous efficacy of 198 lm/W. The photoconversion parameters of the transparent ceramic packaged with a blue light-emitting diode or a laser diode were compared. It was shown that the color temperature of ceramic emissions could be controlled by the spectral width of the excitation beam. Thermally stimulated luminescence was applied to investigate the deep trapping centers imposed by the codopants. A detailed EPR study revealed the presence of F^+, O^-, and Ce^{4+} centers.

DOI: 10.1103/PhysRevApplied.20.014047

I. INTRODUCTION

Worldwide efforts are being made to efficiently produce white light in many everyday lighting applications. Electrical lighting sources account for about 1/6 to 1/5 of the world's electricity production [1]. Therefore, the construction of long-lasting and efficient white light-emitting diodes (LEDs) is in high demand [1–3]. The advantages over conventional light sources include their small size, long service life, energy savings, and environmental friendliness [4,5]. A white LED consists of a semiconductor diode [6,7] or a combination of an

*karol@ukw.edu.pl

ultraviolet (UV) or blue light-emitting diode with a luminescent phosphor [1] that converts part of the exciting light into green-yellow and red emission. Phosphor-converted light-emitting diode (PCLED) devices have been shown to suffer from a performance decrease in the course of exploitation. A search for alternative solutions led to the development of phosphor-converted diodes pumped by a blue-light laser (white PCLDs), which could maintain a high power-conversion efficiency, even when applied in high-power and high-brightness lighting devices [3]. Currently, most commercial white PCLEDs are constructed of a blue LED based on (In, Ga)N/GaN multiple quantum wells and a polymeric compound containing $Y_3Al_5O_{12}$:Ce (YAG:Ce) phosphor powder that emits green-yellow light [8]. Blue light from the (In, Ga)N diode excites the green-yellow luminescence from YAG:Ce, which, in turn, is mixed with unabsorbed blue light from the diode itself to produce white light. A serious problem with this concept is the use of organic or silicone resin with a low thermal conductivity coefficient ($k = 0.1$–$0.4\ \mathrm{W\,m^{-1}\,K^{-1}}$) and poor thermal stability [7]. These disadvantages significantly reduce the output power of LED chips under increasing temperatures and continuous laser irradiation [8]. To overcome these drawbacks, fully inorganic color converters have been proposed because of their higher mechanical strength, thermal stability, thermal conductivity, and efficiency. Inorganic color converters can be divided into three categories: glass ceramics ($k \sim 1.0\ \mathrm{W\,m^{-1}\,K^{1}}$) [9,10], single crystals ($k \sim 9.0$–$15.0\ \mathrm{W\,m^{-1}\,K^{-1}}$) [11,12], and transparent ceramics ($k > 10.0\ \mathrm{W\,m^{-1}\,K^{-1}}$) [13,14]. Among these types of materials, transparent ceramics are the most promising because of their low cost, well-mastered preparation technology, ease of doping, and the possibility of designing integrated devices. Therefore, they have become research hotspots in solid-state lighting. However, the YAG:Ce phosphor combined with the blue-light-emitting chip generates white light with a rather low color rendering index (CRI) and high correlated color temperature (CCT), which bring limitations to its applications. The white light obtained is too cold, and the CRI is too low for indoor illumination [10,11]. Hence, to obtain warm-white light, the addition of a red-light component to a yellow-emitting YAG:Ce phosphor is strongly required.

The composition-engineering strategy based on the replacement of smaller Y atoms with larger Gd (Tb) elements and Al atoms with Ga (Sc) atoms appears to be a good solution [15,16]. In fact, an atom admixture with a larger ionic radius significantly shifts the Ce^{3+} emission to lower energy and increases the contribution of red light, thus improving the CRI and CCT [15,16]. However, this strategy significantly reduces the thermal stability of Ce^{3+} emission in the $(Gd, Tb, Y)_3(Al, Ga, Sc)_5O_{12}$:Ce host and increases the cost of production. Consequently, in such a complex system, the Ce^{3+} luminescence-quenching process begins at significantly lower temperatures [17–19]. Another way is to codope YAG:Ce with ions such as Cr^{3+}, Pr^{3+}, and Mn^{2+}, which can be efficiently sensitized by Ce^{3+} ions and contribute to red emission [20–22]. Codoped red-light-emitting ions can significantly improve both the CRI and CCT by producing warm-white light with the excellent thermal stability of Ce^{3+} luminescence. Despite promising parameters, the quality of light emitted from the codoped samples still exhibits some downsides. Specifically, unevenly distributed luminescent ions in the host can cause an undesired color-temperature deviation. Although photoconversion properties can be improved in different ways by altering the conformal coating structure [23], the composite structure [2,24], and the discharge surface [25], the complexity and high production costs of such materials prevent them from being widely used. Therefore, there is a high demand to find a simple and low-cost production process that enables favorable optical properties to be obtained. An alternative approach to improve the parameters of white PCLED and PCLD is based on the formation of light-scattering centers that can be easily incorporated into the phosphor [26–28]. The light-scattering properties of the phosphors can be enhanced by the incorporation of pores or secondary phases or by tailoring the microstructure with different grain sizes. As a result, exciting radiation propagation is more diffusive, thus significantly eliminating problems in lighting applications associated with LEDs, such as lighting hot spots and angular color distribution [26–28]. However, pores in YAG:Ce ceramics can significantly decrease thermal conductivity [29], excluding their application in high-power solid-state lighting. Furthermore, the cubic structure of $Y_3Al_5O_{12}$ makes it extremely difficult to induce light-scattering effects based on different sizes of phosphor grains and different orientations of their crystallographic axes in space. Therefore, the formation of secondary-phase inclusions, along with red-light-emitting codopants, is considered to be the most effective and practical approach to introduce light-scattering centers into YAG:Ce ceramics.

The present research discusses the influence of codoping with lanthanides (Ln = Er, Ho, Nd, and Pr) and a transition metal (Cr) on the luminescent properties of the YAG:Ce phosphor. These codopants are assumed to act as red-light emitters and may be effectively sensitized by Ce^{3+} ions. In addition, this study reveals the role of light-scattering centers in diffusive light transport in YAG:Ce ceramics. One of the possible sources of light-scattering centers may be related to the segregation of the dopants on grain boundaries, resulting in Rayleigh scattering. This phenomenon may be attributed to the different ionic radiuses of Ln^{3+} or Cr^{3+} ions compared to Y^{3+} and Al^{3+}. The other type of light-scattering center is presented by secondary-phase inclusions, which are the result of introducing nonstoichiometry into the system. Earlier studies showed that garnets had an exceptional tolerance for the solubility of excess lanthanide oxides (Ln_2O_3) [30,31]. This means

that the addition of excess Ln_2O_3 does not alter the stoichiometry of the garnet structure, thus maintaining a single garnet phase. The main mechanism for accommodating deviations from stoichiometry (excess Ln_2O_3) is the formation of antisite defects as well as cation and oxygen vacancies [32]. This suggests that the nonstoichiometry caused by the excess Ln_2O_3 component can increase the concentration of defects, resulting in a decline in the material's overall performance. In contrast, the depletion of the Ln_2O_3 component in $Ln_3Al_5O_{12}$ results in an excess of Al_2O_3. During the sintering process, this surplus Al_2O_3 can be incorporated into the YAG matrix, thereby facilitating the formation of the desired light-scattering centers. In the present study, YAG:Ce, Nd and YAG:Ce, Cr ceramics were fabricated as nonstoichiometric materials, allowing us to test a different design in the formation of this type of light-scattering center. The factors mentioned above may improve the white-light quality of phosphors for solid-state lighting. Here, we establish the optimal concentration ratio of Ce, Ln and Ce, Cr in transparent YAG ceramics for white LEDs and find the correlation between transparency (i.e., light diffusion) and the photoconversion properties of Ln and Cr codoped YAG:Ce. The microstructure, phase purity, absorption, transmittance, and luminescence properties, as well as energy-transfer processes between Ce and codopants, are systematically investigated. Furthermore, the chromaticity parameters of transparent ceramic-based white PCLEDs are estimated. Data on the temperature stability of Ce^{3+} emission are reported for the temperature range of 77–750 K. The effect of codoping on the formation of defects in transparent ceramics is revealed.

II. RESEARCH METHODOLOGY

A. Preparation of transparent ceramics

Transparent YAG ceramics singly doped with cerium (1.0 at.% Ce) or codoped with cerium (1.0 at.%) and lanthanides Er, Ho, and Pr at the level of 0.5 at.% were selected for the present study. The YAG:Ce, Nd (Nd = 0.425 at.%) ceramic samples were prepared with a nonstoichiometric quantity of Nd, according to the nominal chemical composition $Y_{2.955}Ce_{0.03}Nd_{0.0135}Al_5O_{12}$. The YAG:Ce, Cr (Cr = 0.3 at.%) sample was prepared with a 0.5% depletion of Y_2O_3, according to the nominal chemical composition $Y_{2.955}Ce_{0.03}Cr_{0.009}Al_5O_{12}$. First, aqueous slurries of yttrium oxide (99.9% purity), aluminum oxide (99.99% purity), and cerium oxide (99.9% purity) were prepared by mixing the powders in a planetary mill in water with DolapixCE 64 dispersing agent, DuramaxB-1000 binder, and a laboratory-prepared octaanion sintering aid. When samples were codoped with Ln or Cr ions, an appropriate oxide, such as erbium oxide, holmium oxide, neodymium oxide, praseodymium oxide, or chromium oxide, was used to substitute Y_2O_3 (Ln_2O_3 oxides) or Al_2O_3 (Cr_2O_3 oxide). The homogenized aqueous slurries were sprayed into liquid nitrogen to form granules, which were then lyophilized overnight in a freeze dryer. The obtained granulates were uniaxially pressed into disk-shaped samples 20 mm in diameter and a few mm thick and further densified using a cold isostatic pressing process. The samples were calcined in air at 950 °C to remove organic additives and then sintered under vacuum at 1715 °C for 6 h. The samples were annealed in air at 1600 °C for 2 h to reduce the oxygen-vacancy concentration. Ceramics were cut, ground, and polished to obtain samples with dimensions of $4 \times 4 \times 1$ mm^3 and mirrorlike parallel surfaces.

B. Powder XRD and SEM-HRTEM-EDS analysis

The qualitative phase analysis of the ceramics was performed using powder x-ray diffraction (PXRD). Measurements were carried out on a Rigaku SmartLab 3-kW x-ray diffractometer equipped with a copper x-ray tube, operating at 40 kV and 30 mA, and a D/tex Ultra 250 solid-state detector. Phase analysis was performed on bulk samples in continuous mode in Bragg-Brentano geometry ($\theta/2\theta$ scan) over an angular range of 5°–120° (2θ) with a scan step of 0.01° and a speed of 1.2°/min. To reveal grain boundaries for microscopic analysis, the samples were thermally etched in air at 1600 °C for 30 min. The microstructures of the ceramics were studied with a scanning electron microscope (SEM) (Carl Zeiss CrossBeam Workstation AURIGA, Oberkochen, Germany). Structure analysis was carried out with a JEOL JEM-2100 transmission electron microscope (TEM) using an accelerating voltage of 200 kV. The microscope was equipped with an energy-dispersive spectroscopy (EDS) detector and enabled operation in scanning mode (STEM). High-resolution transmission electron microscopy (HRTEM) measurements were made using the lift-out method with a focused gallium-ion beam (FIB). For the HRTEM study, the sample surface was prepared by etching with an argon-ion beam. All measurements were carried out at 300 K.

C. Optical, luminescence, and photoconversion measurements

Absorption and transmittance spectra were recorded with a Jasco V-730 UV-vis spectrometer in the 200–1100 nm spectral range at 300 K. Photoluminescence-excitation (PLE) and -emission (PL) spectra at 300 K were recorded with an Edinburgh Instruments FLS1000 spectrofluorometer, equipped with a 150-W xenon lamp as an excitation source. The recorded spectra were corrected for the spectral transmission and detector sensitivity of the setup. A pulsed nanoLED was used for fast PL-decay-kinetics measurements. The decay curves were recorded using the time-correlated single-photon-counting method.

For measurements of the temperature dependences of emission and excitation spectra, the samples YAG:Ce, YAG:Ce, Nd, YAG:Ce, Cr, and YAG:Ce, Pr were mounted in a JANIS VPF-800 cryostat. Excitation was accomplished with a 400-W deuterium discharge lamp (DDS-400) through a double-quartz prism monochromator (DMR-4). An ARC SpectraPro 300i grating monochromator equipped with a H8259-01 photon-counting head was used to analyze luminescence. The temperature dependences of emission spectra of YAG:Ce, Er and YAG:Ce, Ho ceramics were measured with an Edinburgh Instruments FLS1000 spectrofluorometer with a Janis continuous-closed-cycle refrigerator cryostat.

PLE and PL spectra together with the PL decay curves were recorded by using a custom-made 5000M spectrofluorometer (Horiba Jobin Yvon, Wildwood, MA, USA) using a steady-state laser-driven xenon lamp (Energetiq, a Hamamatsu Company) and nanosecond nanoLED pulsed-light sources in time-correlated single-photon-counting mode (Horiba Scientific) as the excitation sources, respectively. The detection part of the setup involved a single-grating monochromator and a photon-counting detector (TBX-04) (Hamamatsu). The PL and PLE spectra were corrected for experimental distortion. The convolution procedure was applied to the photoluminescence-decay curves to determine true decay times (SpectraSolve software package, Ames Photonics). Temperature-dependent measurements were accomplished by using liquid-nitrogen bath cryostats (Oxford Instruments or LakeShore Cryotronics, environment by Janis). The time-resolved afterglow measurements were performed within a time window ranging from 0 to 600 s after irradiation with a xenon flashlamp at 450-nm wavelength for 5 min using a custom-made 5000M spectrofluorometer (Horiba Jobin Yvon, Wildwood, MA, USA).

Photoconversion experiments were performed by placing ceramic samples on a collimator lens. The beams of the 445-nm laser diode of a CNI laser (FWHM = 2.1 nm) and a 455-nm LED (FWHM = 21.6 nm) were used as excitation sources. The optical power of blue excitation was set to 0.1 W. The beams were coupled to an optical fiber to homogenize exciting radiation. The measurements were performed with a gigahertz BTS-256LED spectrometer equipped with an integrating sphere (for chromaticity parameters) and Avantes USB-2000 spectrometer (spectra). The CIE 1931 coordinates (x,y, CRI) and correlated color temperature were calculated using the S-BTS256 software. All measurements were performed at 300 K.

D. Thermoluminescence measurements

Thermoluminescence measurements in the 300–670 K temperature range were performed using a Risø DA-15 TL reader with a heating rate of 1 K/s. The samples were irradiated with about 12-eV vacuum ultraviolet (VUV) photons.

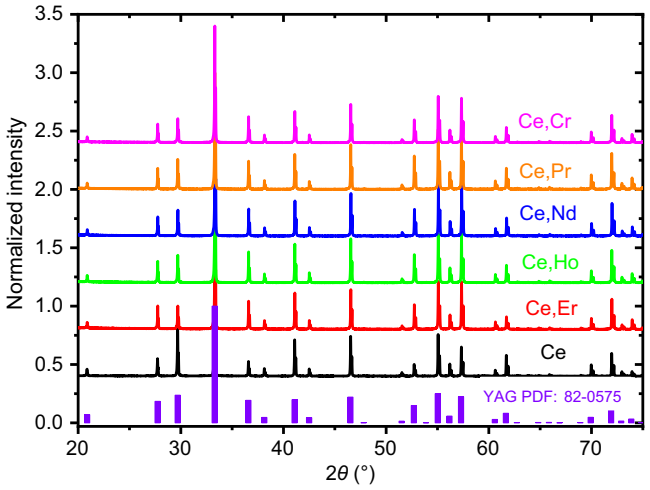

FIG. 1. Theoretical and experimental PXRD patterns for YAG:Ce and YAG:Ce, Ln or Cr ($Ln^{3+} = Er^{3+}$, Ho^{3+}, Nd^{3+}, Pr^{3+}, Cr^{3+}) transparent ceramics recorded at 300 K.

E. Electron paramagnetic resonance analysis

EPR measurements were performed with a commercial Bruker EMXplus spectrometer in the X band (9.4 GHz, resonator type ER4122SHQE, TE011 mode) within the 4–296 K temperature range using an Oxford Instruments ESR900 cryostat. The sample was placed into a quartz tube. The x-ray irradiation of samples in the quartz tube was performed at room temperature and liquid-nitrogen temperature using ISO-DEBYEFLEX 3003 highly stabilized x-ray equipment for structure analysis (tungsten x-ray tube, 50 kV, 30 mA).

III. RESULTS AND DISCUSSION

A. Ceramics phase, nanostructure, and microstructure

Figure 1 shows the PXRD patterns of YAG:Ce transparent ceramics codoped with Er^{3+}, Ho^{3+}, Nd^{3+}, Pr^{3+}, and Cr^{3+} ions. In the codoped and nonstoichiometric samples, the crystal structure is maintained, as confirmed by comparison with reference data: PDF No. 82-575. All samples crystallized in the pure cubic space group Ia-$3d$ (No. 230) without the detectable presence of Al_2O_3, Y_2O_3, $YAlO_3$, $Y_4Al_2O_9$, or $Ln_3Al_2O_6$ aluminate phases. This confirmed that codoping with various Ln^{3+} and Cr^{3+} ions, as well as the introduction of slight nonstoichiometry, did not significantly influence the phase-formation process during the reactive sintering stage. However, the presence of secondary phases below 2% was beyond the detection limit of the PXRD method [33]. Therefore, other techniques more sensitive to morphology, such as SEM-EDS, need to be

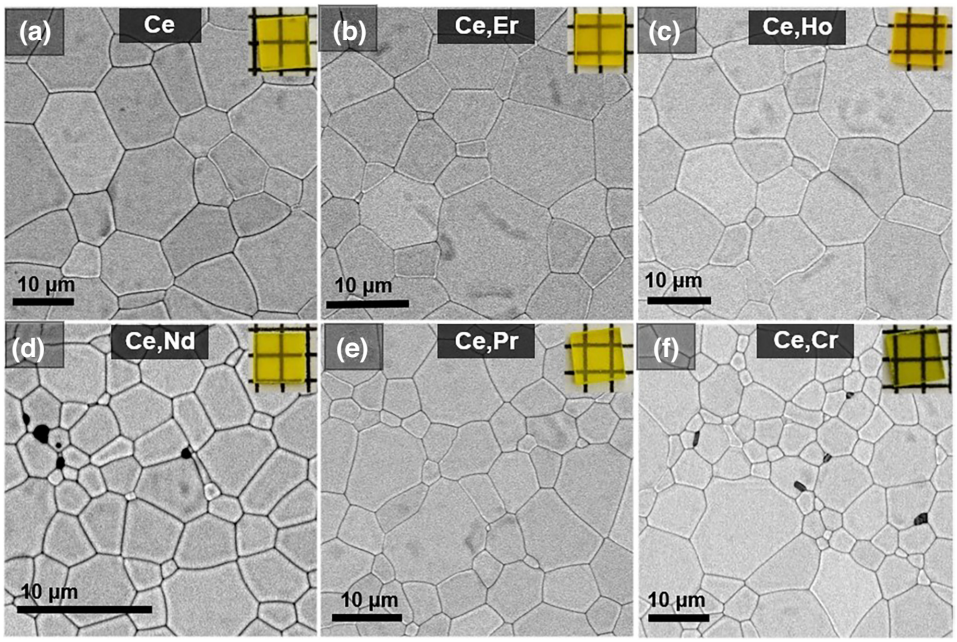

FIG. 2. SEM microimages of mirror-polished YAG transparent ceramics doped with (a) Ce 1.0%, and codoped with (b) Ce 1.0%, Er 0.5%; (c) Ce 1.0%, Ho 0.5%; (d) Ce 1.0%, Nd 0.425%; (e) Ce 1.0%, Pr 0.5%; (f) Ce 1.0%, Cr 0.3%. Insets depict fragments of mirror-polished specimens.

applied to detect smaller amounts of inclusions (Figs. 2 and 3).

Figure 2 shows the SEM microimages of mirror-polished ceramics. All ceramics were highly dense and pore free with regular grain boundaries. The average grain size was between 3.9 and about 10 μm, see the Supplemental Material for the grain size distribution in Table S1 [63]. The YAG:Ce^{3+} transparent ceramics [Fig. 2(a)] and YAG:Ce^{3+}, Er^{3+} [Fig. 2(b)], YAG:Ce^{3+}, Ho^{3+} [Fig. 2(c)], and YAG:Ce^{3+}, Pr^{3+} [Fig. 2(e)] codoped ceramics do not contain light-scattering centers in the form of secondary-phase inclusions. It should be noted that all samples exhibit surface roughness, even after the polishing step. However, all of them were prepared in the same manner; hence, the eventual transmittance drop attributed to the surface finish could be treated as a systematic error. Inducing nonstoichiometry in YAG:Ce^{3+} transparent ceramics codoped with both Nd^{3+} and Cr^{3+} ions resulted in the formation of small and irregularly shaped secondary-phase inclusions well incorporated into the ceramic structure [see black spots in Figs. 2(d) and 2(f)]. The insets in Fig. 2 suggest that all the prepared samples show good transparency, even in the case of nonstoichiometric YAG:Ce, Nd and YAG:Ce, Cr samples.

Figure 3 shows the elemental distribution in the selected samples: (a) YAG:Ce 1.0%, Er 0.5% (stoichiometric), (b) YAG:Ce 1.0%, Cr 0.3%, and (c) YAG:Ce 1.0%, Nd 0.425% (nonstoichiometric) transparent ceramics. The EDS mapping results for YAG:Ce^{3+} 1.0%, Er^{3+} 0.5% showed a uniform distribution of O, Al, Y, Ce, and Er atoms in ceramics. This indicated that the solid-state reactive sintering process using the selected parameters ensures proper diffusion and resulted in the extraction of homogeneous material. The same results were observed for YAG:Ce^{3+} 1.0% and samples codoped with Ho^{3+} and Pr^{3+} ions. The nonstoichiometry introduced in the YAG:Ce, Cr and YAG:Ce, Nd samples resulted in the successful formation of the desired light-scattering centers, significantly disrupting the uniform distribution of atoms. The EDS elemental mapping results for the O and Al atoms showed spots with a brighter shade, while that for the Y atoms showed black spots at the same location [Figs. 3(b) and 3(c)]. Specifically, the bright spots on the EDS maps were related to an increase in the intensity of the signals corresponding to O and Al atoms. The black spots reflected the lack or lower content of Y atoms [34]. This revealed that secondary-phase inclusions consisted of O and Al atoms that formed the Al_2O_3 phase. This result showed that the formed ceramic structure had well-incorporated light-scattering centers that could enable diffusive light propagation. Another significant observation was a higher concentration of Al_2O_3 phase inclusions in the YAG:Ce, Cr sample compared to the YAG:Ce, Nd sample. This disparity could be attributed to the degree of nonstoichiometry present in each sample. Consequently, it could be concluded that the concentration of Al_2O_3 phase inclusions could be effectively controlled by tailoring the degree of depletion of one component.

Figure 4(a) shows an HRTEM image of the grain boundary between two grains in YAG:Ce 1.0% ceramics. The inset shows a thin interface layer of less than 1 nm wide with a significantly disordered structure. To confirm the segregation of Ce^{3+} ions toward the grain boundary, point-by-point EDS measurements were performed using scanning mode of the transmission electron microscope. Figure 4(b) (left side) shows spectra recorded on the line crossing

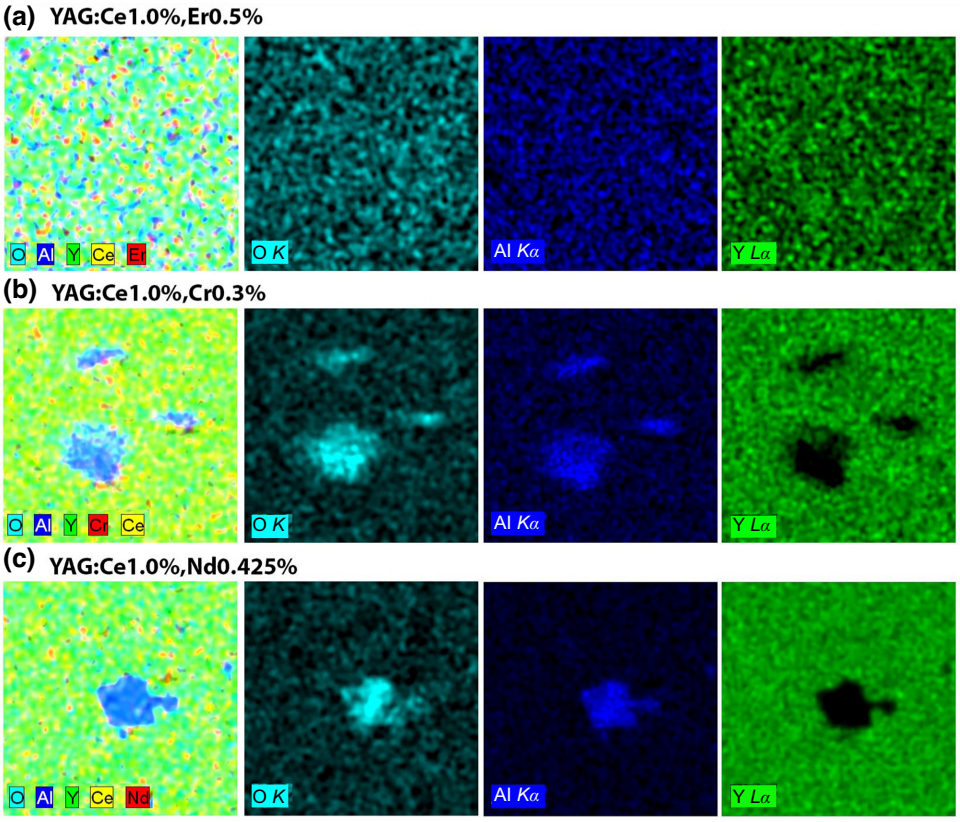

FIG. 3. EDS elemental mapping of selected areas in (a) YAG:Ce 1.0%, Er 0.5%; (b) nonstoichiometric YAG:Ce 1.0%, Cr 0.3%; and (c) nonstoichiometric YAG:Ce 1.0%, Nd 0.425% transparent ceramics. Lighter spots indicate an increase in the content of atoms in the analyzed area, whereas black spots represent a lack of respective atoms locally. $T = 300$ K.

both grains and their boundary (the overall distance covered by the measurement was ca. 50 nm). The right side of Fig. 4(b) presents a graph of the intensity of the Ce $L\alpha$ x-ray fluorescence line recorded in the area studied. It is seen that the increase of the signal corresponding to the Ce $L\alpha$ fluorescence line is observed just on the grain boundary. The higher number of counts demonstrates an increased content of Ce atoms. These data confirmed that the highest concentration of Ce^{3+} ions was spatially located at the grain boundary, which was consistent with previous research on the distribution of dopants in the YAG host [35]. This observation is further supported by the absorption and photoluminescence analyses (Sects. III B and III C).

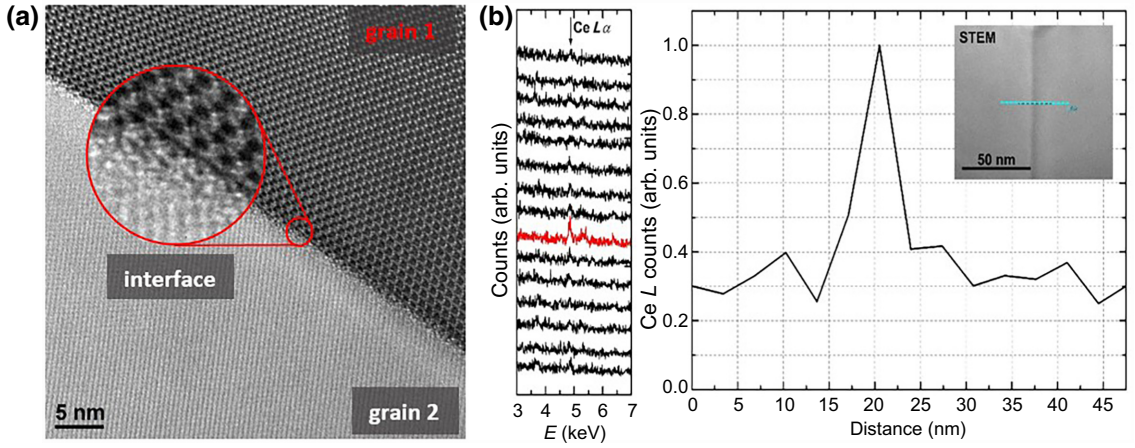

FIG. 4. (a) HRTEM image of grain boundaries 1 and 2 in YAG:Ce 1.0% ceramics; (b) point-by-point EDS measurements carried out along a line perpendicular to the grain boundaries. Graph in the left part shows the fragments of fluorescence spectra in the vicinity of the Ce $L\alpha$ x-ray line. Spectrum with the highest fluorescence intensity of this peak is marked in red. Image to the right shows the number of counts of the Ce $L\alpha$ line at each measured point. Line in the inset shows the extent of the STEM scan.

B. Transmittance and absorption properties

Figure 5(a) shows the transmittance spectra of the ceramics obtained. It can be seen that both Ho^{3+} and Pr^{3+} codoped YAG:Ce^{3+} samples are highly transparent, with 76% and 77% optical transmittance at 900 nm, respectively. The optical transparency for YAG:Ce^{3+} ceramics is around 68%. Furthermore, the transmittance gradually decreases in the incident wavelength range from 800 to 530 nm, which is tentatively assigned to the formation of nanodefects. When the size of the nanodefects in ceramics is smaller than the wavelength of the incident radiation, Rayleigh scattering occurs with an intensity proportional to $1/\lambda$ [36]. The flatter transmittance curve for the Ho^{3+} and Pr^{3+} codoped samples indicates that the nanodefect content in these samples is much lower than that of YAG:Ce^{3+} ceramics. Nanodefects can originate from local lattice strains caused by increased segregation of Ce^{3+} or other RE^{3+} (RE is rare earth) ions to grain boundaries, where the Ce-Ce or Ce-RE clusters can be formed. Additionally, nanodefects can be formed in a disordered interface between grains. This hypothesis is supported by HRTEM nanostructure analysis. The presence of nanodefects may have two different causes. The first is the behavior of the dopant itself. Depending on the oxidation state under vacuum sintering conditions, dopant ions in ceramics may also exist in several oxidation states. This results in the generation of point defects, namely, vacancies. The presence of vacancies can increase diffusion in the system, resulting in an improved homogenization and densification process of ceramics. The second cause is a technological one, since the dopant powders exhibit different morphology (shape, size of crystallites and agglomerates, appearance of sintering necks between the crystallites in powder agglomerates, etc.). This factor can affect the distribution of dopants in the bulk, resulting in different optical qualities of the ceramics. The most significant example of this effect in the present study was shown by a YAG:Ce, Er sample, which was prepared using the rather coarse Er_2O_3 powder (see Fig. S1 within the Supplemental Material [63] for the shape and size of crystallites in raw powders). Although the powder was additionally milled before preparation of the suspension, the transmittance of the sample was significantly lower compared to that of other stoichiometric samples.

In the nonstoichiometric samples, the optical transmittance was significantly reduced to 33% and 62% at 900 nm in the codoped ceramics with Nd^{3+} and Cr^{3+}, respectively. The decrease in transmittance in these two samples was mainly attributed to the introduction of secondary-phase inclusions, but not to the influence of codoping itself (see Fig. 3). These inclusions can significantly enhance lattice stress, increase the number of oxygen vacancies, and facilitate the formation of particular types of defects [e.g., antisite defects, Y in the Al site (Y_{Al}) and nanodefects] [17,18]. The optical transmittance of the Ce^{3+}-doped and Ln^{3+},Cr^{3+} codoped YAG ceramics was close to 0% between 190 and 350 nm, while the undoped YAG sample showed high transparency in this spectral region. This observation may suggest that Ce^{3+} doping and Ln^{3+},Cr^{3+} codoping are responsible for the formation of oxygen vacancies and other lattice defects [37,38]. This hypothesis is further supported by the analysis of photoluminescence and thermally stimulated luminescence (TSL) data (see Figs. 6 and 7). During the ceramic sintering process performed at high temperatures and the subsequent air annealing process, part of the Ce^{3+} ions can be oxidized to the Ce^{4+} state. Regardless of the smaller ionic radius of $Ce^{4+}_{VIII} = 0.970$ Å than $Ce^{3+}_{VIII} = 1.134$ Å [39], it is believed that Ce^{4+} imposes additional lattice distortion and lattice stress, as charge compensation that involves the creation of charged point defects, vacancies, or interstitials, and even more complex defect clusters (in

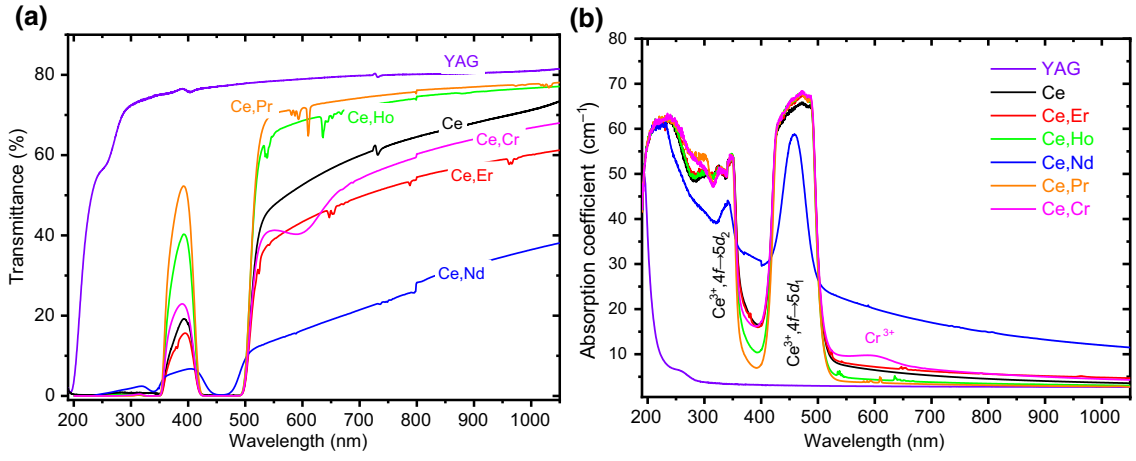

FIG. 5. (a) Optical transmittance spectra and (b) absorption spectra for Ce-doped and Ln, Cr codoped YAG:Ce transparent ceramics at $T = 300$ K. Undoped YAG transparent ceramic is a reference sample.

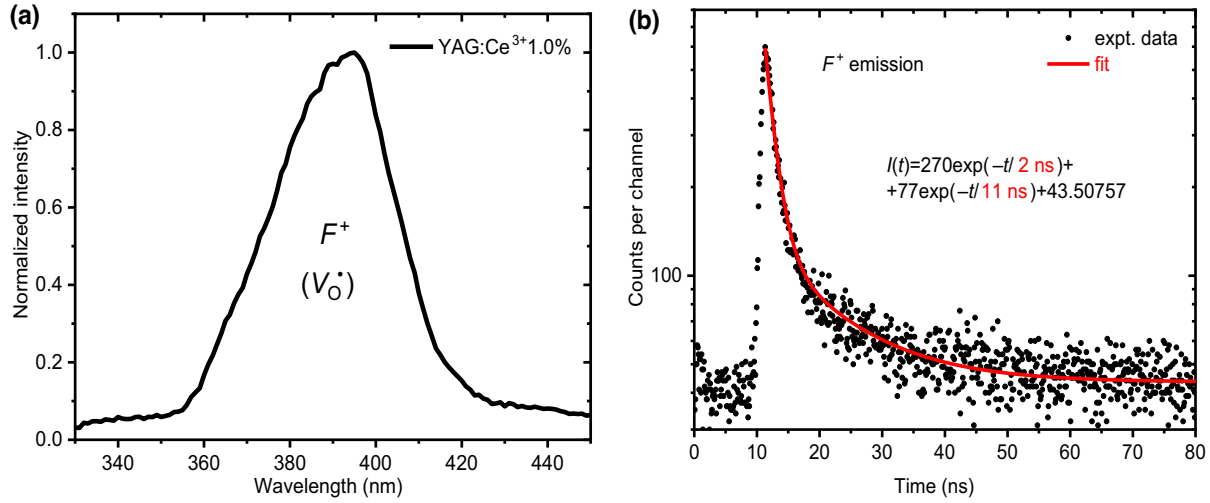

FIG. 6. (a) Photoluminescence-emission spectrum of F^+ center excited at 260 nm, and (b) photoluminescence-decay kinetics of F^+ center at 395 nm excited by 260 nm at $T = 300$ K.

particular, defect pairs), are needed for it. The nature and concentration of defects depend on the specific charge imbalance locally and the relative position of the structure of the defect energy levels in the host electronic band [34]. Consequently, the Ce^{4+} ion and point defects (oxygen vacancy) can strongly absorb radiation in the UV spectral range. This assumption is supported by the absorption spectra displayed in Fig. 5(b). Specifically, strong absorption between 200 and 300 nm can be attributed to the $O^{2-} \rightarrow Ce^{4+}$ charge-transfer transition, that is, electron transfer between the O $2p$ and Ce $4f$ energy levels [34]. Stabilization of Ce^{4+} ions in the YAG host lattice can be achieved by the formation of oxygen vacancies. The presence of oxygen vacancies is fingerprinted by the characteristic F^+ luminescence (an oxygen vacancy with one trapped electron) [40,41] [see Figs. 6(a) and 6(b) in Sec. III A]. Therefore, the high-energy absorption bands can be attributed to both the Ce^{4+} charge-transfer transition and higher-energy Ce^{3+} $4f \rightarrow 5d3,4$ absorption [42]. Strong absorption bands, located at 340 and 455 nm, belong to the $4f \rightarrow 5d2$ and $4f \rightarrow 5d1$ electron transitions in Ce^{3+} ions, respectively [43]. The $4f \rightarrow 5d1$ absorption band at 455 nm for highly transparent ceramics (i.e., Er^{3+}, Ho^{3+}, Pr^{3+}, Cr^{3+} codoped YAG:Ce^{3+}) is saturated mainly due to the high concentration of Ce^{3+} ions. This effect can also be enhanced by segregating Ce^{3+} ions near the disordered interface between grains [43–45]. The $4f \rightarrow 5d1$ absorption band at 455 nm in Nd^{3+} codoped YAG:Ce^{3+} ceramic (nonstoichiometric composition) shows a slightly lower intensity. This observation is due to the lower optical transmittance of the sample. In the YAG:Ce, Cr ceramics, an additional broad spin-allowed $4A2 \rightarrow 4T2$ absorption transition of Cr^{3+} is revealed at 620 nm [46]. Low-intensity absorption lines corresponding to the $4f \rightarrow 4f$ transitions of Er^{3+}, Ho^{3+}, and Pr^{3+} are also observed between 500 and 700 nm in the absorption spectra of YAG:Ce^{3+} codoped ceramics.

C. Photoluminescence characteristics

Figure 8(a) displays the room-temperature photoluminescence-excitation spectra for Ce^{3+} luminescence at 550 nm in transparent YAG:Ce ceramics codoped with Ln^{3+},Cr^{3+} ions. The excitation spectra are in agreement with the absorption spectra [Fig. 5(b)] and consist of two broad bands associated with electron transitions in Ce^{3+} ions. The band centered at 455 nm corresponds to the $4f \rightarrow 5d1$ transition, while the excitation at 340 nm is attributed to the $4f \rightarrow 5d2$ transition [43]. The Ce^{3+} $4f \rightarrow 5d1$ excitation bands show saturation similar to that observed for the absorption bands. In addition to Ce^{3+}-related

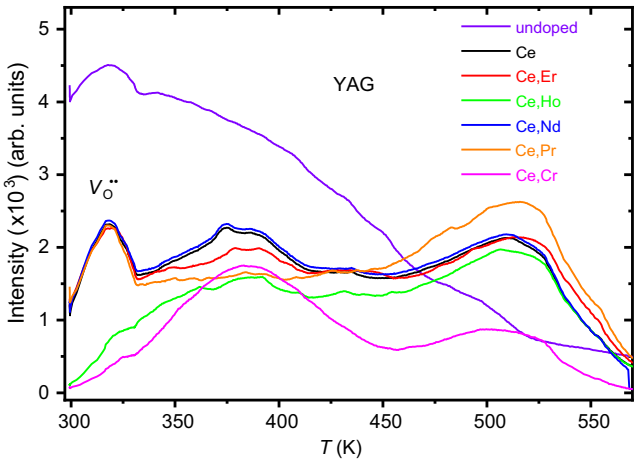

FIG. 7. TSL glow curves of Ce^{3+}-doped and Ln^{3+},Cr^{3+} codoped YAG:Ce^{3+} transparent ceramics irradiated by 12-eV VUV photons at room temperature.

TABLE I. Decay constants for Ce^{3+} emission in Ce^{3+}-doped and Ln^{3+},Cr^{3+} codoped YAG:Ce^{3+} transparent ceramics. The abbreviation frac. tot. int. represents the fraction of the total intensity.

Chemical composition Ce^{3+} 1.0%, Ln^{3+}(Cr^{3+})	Decay constants	
	τ_1 [ns]/frac. tot. int.	τ_2 [ns]/frac. tot. int.
YAG:Ce^{3+}	68/1.0	–
YAG:Ce^{3+}, Er^{3+} (0.5%)	53/0.98	11/0.02
YAG:Ce^{3+}, Ho^{3+} (0.5%)	58/0.93	16/0.07
YAG:Ce^{3+}, Nd^{3+} (0.425%)	62/0.98	22/0.02
YAG:Ce^{3+}, Pr^{3+} (0.5%)	55/0.96	13/0.04
YAG:Ce^{3+}, Cr^{3+} (0.3%)	44/0.82	12/0.18

excitation bands, Pr codoped YAG:Ce^{3+} also shows a broad band centered at 290 nm. This band is attributed to the Pr^{3+} $4f \rightarrow 5d1$ electron transition, and its presence indicates $Pr^{3+} \rightarrow Ce^{3+}$ energy transfer [47]. Figure 8(b) shows the emission spectra of the Ce^{3+}-doped and Ln^{3+},Cr^{3+} codoped YAG:Ce^{3+} transparent ceramics excited at 450 nm, corresponding to the Ce^{3+} $4f \rightarrow 5d1$ transition. The broad band centered at 550 nm belongs to the $5d1 \rightarrow 4f$ emission transition of Ce^{3+} ions. The appearance of emission lines at 610, 630, and 640 nm in YAG:Ce, Pr ceramics is caused by the $1D2 \rightarrow 3H4$, $3P0 \rightarrow 3H6$, and $3P0 \rightarrow 3F2$ transitions in the Pr^{3+} ion, respectively. The narrow dips in the Ce^{3+} luminescence prove the $Ce^{3+} \rightarrow Pr^{3+}$ radiative energy transfer. The emission bands between 650 and 780 nm in the YAG:Ce^{3+}, Cr^{3+} sample belong to the $2E \rightarrow 4A2$ and $2E \rightarrow 4A2$ electron transitions in Cr^{3+} ions [48]. Furthermore, the wide dip in the Ce^{3+} emission between 560 and 640 nm is evidence of radiative energy transfer from Ce^{3+} to Cr^{3+} ions, as Cr^{3+} ions are efficiently excited in this spectral range [see Fig. 9(a)]. This demonstrates that, due to the overlap of Ce^{3+} emission and codopant absorption, both Pr^{3+} and Cr^{3+} ions can be efficiently sensitized by Ce^{3+} ions, and therefore, contribute with the desired red emission to the YAG:Ce, Pr and YAG:Ce, Cr photoconverters. It should be stressed that Pr^{3+} and Cr^{3+} ions are also directly excited by the blue LED [48,49]. The dips caused by the codopant absorption are also observed in the Ce^{3+} emission in Er, Ho, and Nd codoped YAG:Ce ceramics, confirming the $Ce^{3+} \rightarrow Er^{3+}$,$Ho^{3+}$,$Nd^{3+}$ radiative energy transfer [Fig. 8(b), inset]. However, the latter codopants do not emit in the red spectral range.

Further evidence of energy transfer from Ce^{3+} ions towards Ln^{3+},Cr^{3+} codopants is provided by the decay kinetics of the Ce^{3+} luminescence (Fig. 10). The decay time values for all samples are summarized in Table I. Each sample was excited with 450-nm pulsed nanosecond LED radiation while monitoring the Ce^{3+} emission at 550 nm. The decay curves were fitted with single- or double-exponential functions according to

$$I(t) = \sum I_i \exp(-t/\tau_i) + B, \; i = 1, 2, \qquad (1)$$

where I is the luminescence intensity, I_i is the initial intensity at 0 ns, t is the time, τ_i is the decay time, and B is the background intensity.

The decay curve for Ce^{3+} luminescence in the YAG:Ce^{3+} sample shows a single-exponential profile with a decay constant around 68 ns, which is slightly longer than the typical Ce^{3+} decay time in YAG:Ce^{3+} with a

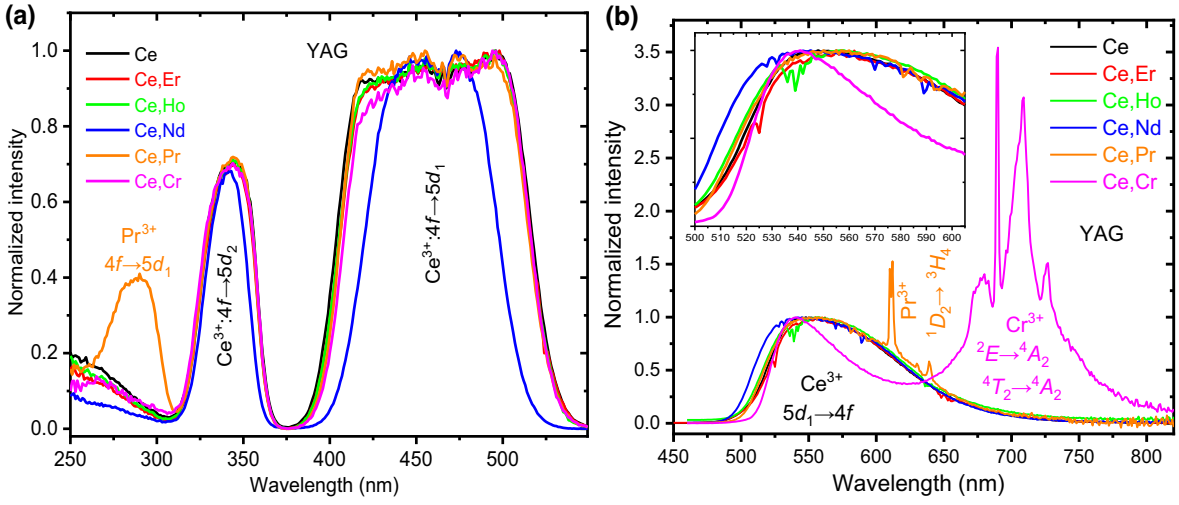

FIG. 8. (a) Photoluminescence-excitation spectra for the Ce^{3+} emission at 550 nm; (b) photoluminescence-emission spectra excited at 450 nm into the $4f \rightarrow 5d1$ absorption band in the Ce^{3+}-doped and Ln^{3+},Cr^{3+} codoped YAG:Ce^{3+} transparent ceramics at $T = 300$ K. Inset shows the Ce^{3+}-related luminescence between 500 and 600 nm to emphasize $Ce^{3+} \rightarrow Ln^{3+}$,$Cr^{3+}$ radiative energy transfer.

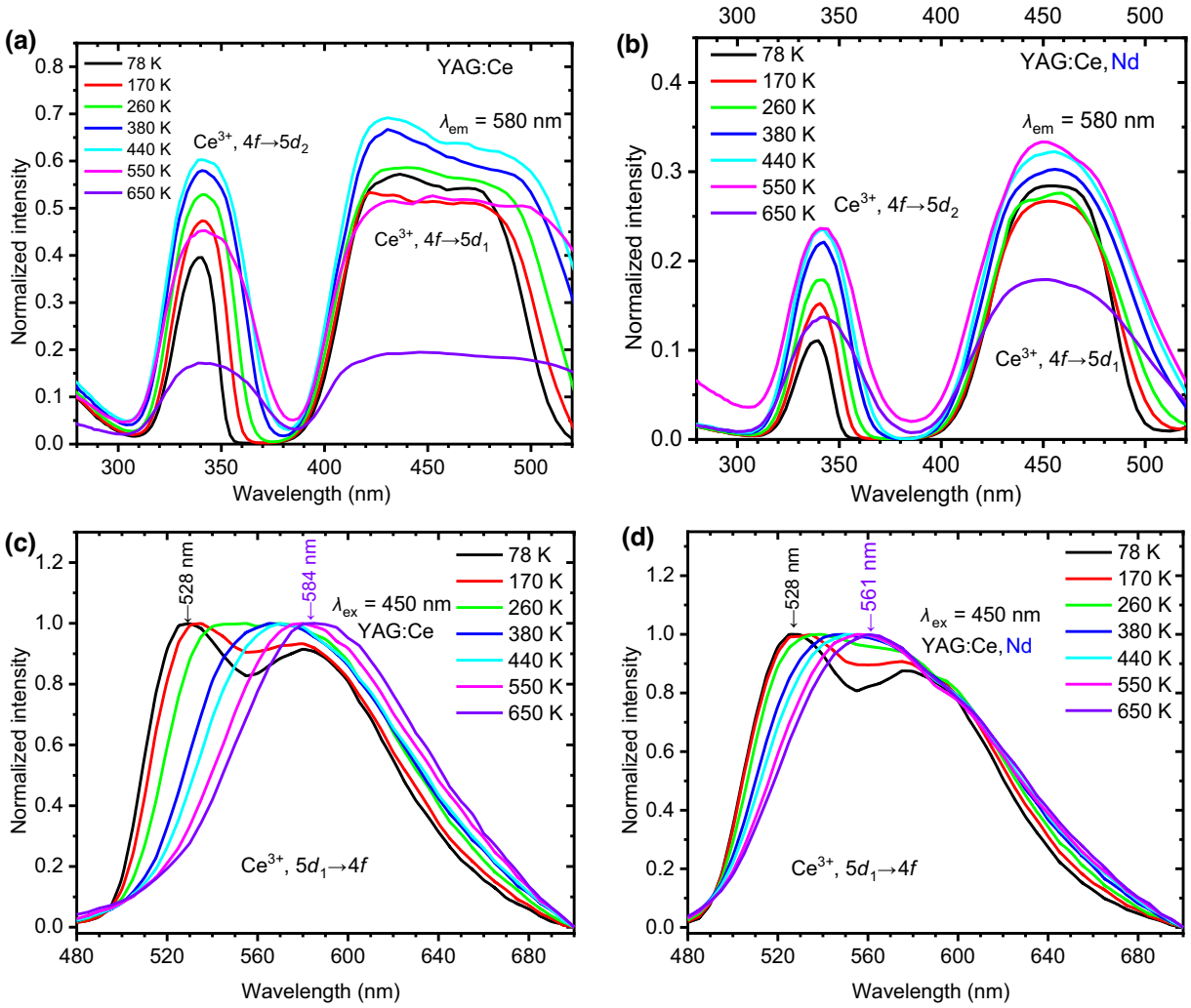

FIG. 9. Photoluminescence-excitation (a),(b) and -emission (c),(d) spectra of Ce^{3+} ions in (a),(c) YAG:Ce and (b),(d) YAG:Ce, Nd ceramics recorded in the temperature range 78–650 K.

lower Ce^{3+} content (i.e., 63 ns for Ce 0.033%) [43]. This increase in the decay time provides evidence that Ce^{3+} ions segregate towards grain boundaries in the YAG host lattice, where they can form Ce^{3+}-Ce^{3+} pairs and allow mutual energy transfer. The increase in the decay time at higher Ce concentration appears due to the reabsorption process (i.e., energy transfer from excited Ce^{3+} ions to nearby perturbed Ce^{3+} ions) [43]. Figure 10 and data in Table I also demonstrate that codoping results in a change of the decay-curve profile of Ce^{3+} luminescence from single exponential to double exponential, whereas one of the components possesses significantly accelerated decay times. The acceleration of the decay times of Ce^{3+} luminescence supports the assumption of the energy-transfer process from Ce^{3+} ions towards Er^{3+}, Ho^{3+}, Nd^{3+}, Pr^{3+}, and Cr^{3+} codopants in the YAG host lattice. The slower components, $\tau_1 = 68-44$ ns, are associated with Ce^{3+} ions that are unperturbed or little perturbed by Ln or Cr atoms. Accelerated components, $\tau_2 = 22-11$ ns, are related to Ce^{3+} ions, which transfer excitation energy to Ln^{3+},Cr^{3+} ions. Additionally, the frac. tot. int. of each component in the overall decay time is calculated by

$$\text{frct.tot.int.} = \frac{I_i \tau_i}{\sum_i I_i \tau_i}, \tag{2}$$

where I_i is the intensity and τ_i is the decay constant of the ith component of the fit.

The weight fraction of each component in ceramics exhibits significant variability, which can impact the efficiency of energy transfer from Ce^{3+} ions to Ln^{3+},Cr^{3+} ions. Notably, the findings indicate that the energy transfer from Ce^{3+} ions to Er^{3+}, Ho^{3+}, and Cr^{3+} codopants is most efficient, as evidenced by the highest weight fractions of these components. Conversely, the weight fractions

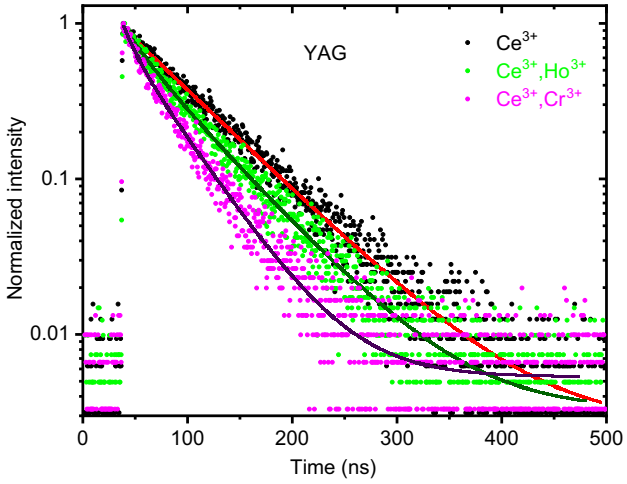

FIG. 10. Photoluminescence-decay kinetics curves of YAG:Ce^{3+}, YAG:Ce^{3+}, Ho^{3+}, and YAG:Ce^{3+}, Cr^{3+} transparent ceramics recorded for Ce^{3+} luminescence at 550 nm under excitation into the $4f \rightarrow 5d1$ 450-nm absorption band of Ce^{3+} at $T = 300$ K.

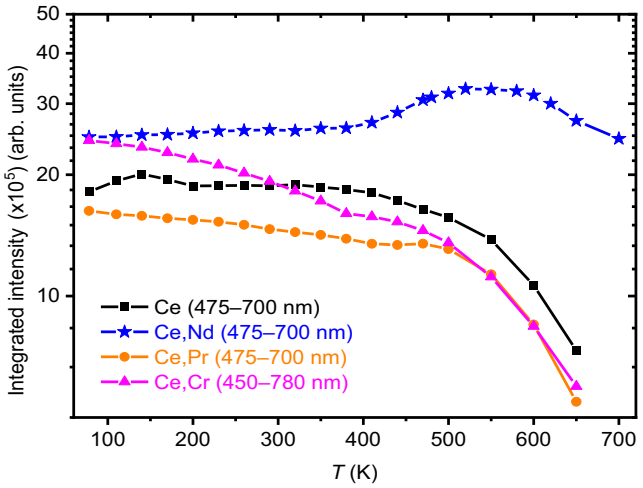

FIG. 11. Temperature dependence of the integrated emission intensity for Ce^{3+}-doped and Nd^{3+}, Pr^{3+}, and Cr^{3+} codoped YAG:Ce ceramics under excitation by 2.75-eV photons (450 nm).

of Nd^{3+} and Pr^{3+} ions indicate the least-efficient energy transfer between these elements and Ce^{3+} ions.

The photoluminescence-emission spectrum of the F^+ center (an oxygen vacancy with one trapped electron, V_O) depicted in Fig. 6(a) can be efficiently excited at wavelengths below 265 nm [47]. The F^+ emission is centered at 395 nm, which is characteristic of this kind of defect-related luminescence in the YAG host lattice [38,39,49]. The decay curve of the F^+ emission [Fig. 6(b)] was fitted with a double-exponential function according to Eq. (1) ($i = 2$). Due to the allowed character of the $1B \rightarrow 1A$ singlet-singlet transition in F^+ centers, the main component of the decay time is around 2 ns [50]. The presence of a slower component, $\tau_2 = 11$ ns, and the irregular shape of the emission band could indicate disturbance or even the aggregation of F^+ centers. It is worth noting that the surrounding Ce^{3+} ions ($4f \rightarrow 5d2$ transition) can absorb the F^+-center-related emission near the short-wavelength side. This might be the reason why the F^+-related emission has an irregular shape. Nevertheless, these results need further research for better understanding.

D. Temperature dependence of emission

For phosphor applications, it is important to evaluate the temperature dependence of the emission from the point of view of its efficiency and spectral characteristics. The photoluminescence characteristics of Ce^{3+}-doped and Nd, Pr, and Cr codoped YAG:Ce ceramics at different temperatures are analyzed in Figs. 9 and 11. The photoluminescence-excitation spectra for the Ce^{3+} emission at 540 nm and the photoluminescence-emission spectra excited at 450 nm in YAG:Ce and YAG:Ce, Nd ceramics were recorded in the temperature range of 77–650 K [Figs. 9(a) and 9(b)]. In the YAG:Ce sample, the excitation and emission bands gradually broaden with increasing temperature, leading to the increase of their spectral overlap, and consequently, to a significant enhancement of energy-transfer processes within the Ce^{3+}-Ce^{3+} pairs. The related increase in the reabsorption rate with temperature may considerably lower the thermal stability of Ce^{3+} luminescence. The temperature-imposed broadening of the 450-nm excitation band in the YAG:Ce^{3+}, Nd^{3+} sample is smaller, leading to less-significant overlap between the excitation and emission bands, resulting in a less-effective reabsorption process.

Figures 9(c) and 9(d) show Ce^{3+} photoluminescence-emission spectra at selected temperatures in YAG:Ce and YAG:Ce, Nd ceramics. At low temperatures, the photoluminescence-emission spectra show well-resolved characteristic doublet peaks corresponding to the transitions from the $5d1$ to $2F5/2$ (shorter-wavelength-band side) and $2F7/2$ (longer-wavelength-band side) spin-orbit states of the Ce^{3+} $4f_1$ electronic structure. When the temperature increases, the two emission bands continuously expand and their overlap becomes more significant [40]. Furthermore, the intensity ratios of the peaks corresponding to the $5d1 \rightarrow 2F5/2$ and $5d1 \rightarrow 2F7/2$ transitions of Ce^{3+} are also temperature dependent. This temperature dependence can be the result of the thermally imposed broadening of both excitation and emission bands [Figs. 9(a) and 9(b)]. This continuous broadening, especially for the excitation bands, causes the reabsorption of the emission corresponding to the $5d1 \rightarrow 2F5/2$ transition by the neighboring Ce^{3+} ions and nonradiative energy transfer to the perturbed Ce^{3+} ions, which emit at slightly lower energy [43,50]. Indeed, the strong reabsorption of the

emission corresponding to the $5d1 \rightarrow 2F5/2$ transition in YAG:Ce and YAG:Ce, Nd ceramics significantly reduces its intensity. Consequently, the $5d1 \rightarrow 2F7/2$ emission transition becomes dominant and has a stronger contribution to the total luminescence ($5d1 \rightarrow 2F5/2 + 2F7/2$). This causes a continuous redshift of the emission-band maximum [Figs. 9(c) and 9(d)]. This process is more pronounced in stoichiometric YAG:Ce ceramics than in nonstoichiometric YAG:Ce, Nd. In stoichiometric YAG:Ce, the maximum emission shifts monotonically by 56 nm from about 528 to 584 nm with increasing temperature, while in nonstoichiometric YAG:Ce, Nd, the shift is only 33 nm from about 528 to 561 nm. A remarkably narrower shape of excitation bands, showing a much weaker effect of saturation and a much smaller displacement of the Ce^{3+} emission band with temperature in nonstoichiometric YAG:Ce, Nd compared to those in YAG:Ce, imply a noticeably lower concentration of Ce^{3+} in YAG phase of YAG:Ce, Nd, probably due to the escape of Ce into the Al_2O_3 phase, where it has different spectral characteristics; see Fig. S2 within the Supplemental Material [63] for Ce^{3+} luminescence in the Al_2O_3 phase [51].

Figure 11 shows integrated Ce^{3+} emission intensity measured as a function of temperature for Ce^{3+}-doped and Nd^{3+}, Pr^{3+}, and Cr^{3+} codoped YAG:Ce^{3+} ceramics. The presented results demonstrate the very complex effect of nonstoichiometry and codoping on the temperature quenching of Ce^{3+} luminescence. In Ce^{3+}-doped and Er^{3+}, Ho^{3+}, Pr^{3+}, and Cr^{3+} codoped YAG:Ce ceramics, the intensity of the Ce^{3+} emission continuously decreases with increasing temperature; see Fig. 11 and Figs. S3 and S4 within the Supplemental Material [63]. To explain this luminescence-quenching process, the influence of the relatively high concentration of Ce^{3+} ions must be considered. Thermally imposed broadening of the excitation and emission bands enhances the absorption strength in the tails of the absorption band. This leads to thermally activated concentration quenching, where energy migrates between Ce^{3+} ions, finally reaching luminescence-quenching centers [43,50]. The mechanism responsible for the quenching of luminescence at higher temperatures is the thermally induced crossover from the excited-state $5d1$ parabola to the ground-state $4f$ parabola [18]. Unlike YAG:Ce, Er, YAG:Ce, Ho, YAG:Ce, Pr, and YAG:Ce, Cr, the nonstoichiometric YAG:Ce, Nd sample shows stable Ce^{3+} emission intensity until around 400 K, whereas it increases significantly further between 425 and 600 K. The quenching process probably starts above 650 K. The variations in spectra and integrated photoluminescence intensity in Ce^{3+}-doped and Er^{3+}, Ho^{3+}, Pr^{3+}, Nd^{3+}, and Cr^{3+} codoped YAG ceramics under excitation by 2.75-eV photons (450 nm) over a temperature range of 77–690 K are shown in Figs. S3 and S4, respectively, within the Supplemental Material [63]. To better understand this unusual temperature behavior, the temperature dependence of the decay kinetics of Ce^{3+} emission in YAG:Ce and YAG:Ce, Nd ceramics was investigated (Fig. 12).

The Ce^{3+} luminescence-decay curves were approximated using a double-exponential function, resulting in the introduction of the mean decay time, τ_m, which is defined by

$$\tau_m = \frac{\sum_i I_i \tau_i^2}{\sum_i I_i \tau_i}, \tag{3}$$

where I_i is the initial intensity and τ_i is the decay constant of the ith component of the fit. The temperature dependence of Ce^{3+} photoluminescence-decay times is consistent with the temperature dependence of emission intensity in the YAG:Ce ceramic [Fig. 12(a)]. However, in the case of the YAG:Ce, Nd ceramic, the temperature dependence of Ce^{3+} decay times shows a distinctly different profile from the temperature dependence of emission intensity. In these ceramics, the beginning of thermal quenching, which influences the decay-time constants, starts at around 500 K, similar to that in YAG:Ce, while the decrease in emission intensity begins at around 650 K. To explain this discrepancy, the photoluminescence-decay-curve backgrounds are compared for YAG:Ce and YAG:Ce, Nd [Fig. 12(b)]. The background obtained from the fit is rather temperature independent in YAG:Ce ceramics. In YAG:Ce, Nd ceramics, the intensity of the decay-curve background increases by 3 orders of magnitude between 300 and 520 K, and by a factor of 2 between 550 and 750 K. The temperature interval, in which the increase in the intensity of the PL background in the decay kinetics experiment is observed, is consistent with that of the increase in PL intensity (see Fig. 11). Such an increase in the background of the PL-decay curves is usually related to the thermoluminescence of the sample or energy-transfer processes from specific types of defects. The temperature interval, in which the background increase is detected, corresponds well also with the 530-K TSL peak observed in the samples irradiated by 12-eV photons (Fig. 7).

Additionally, the Supplemental Material [63] provides a comprehensive analysis of the temperature dependence of the photoluminescence-decay times of Ce^{3+} in YAG:Ce, Er, YAG:Ce, Pr, YAG:Ce, Ho, and YAG:Ce, Cr ceramics, revealing a correlation with the observed temperature dependence in the emission intensity. See Figs. S3–S5 within the Supplemental Material [63] for detailed information regarding this correlation, along with graphical representations.

E. Photoconversion properties

The effects of light-scattering centers on the photoconversion properties in all ceramics were studied using two

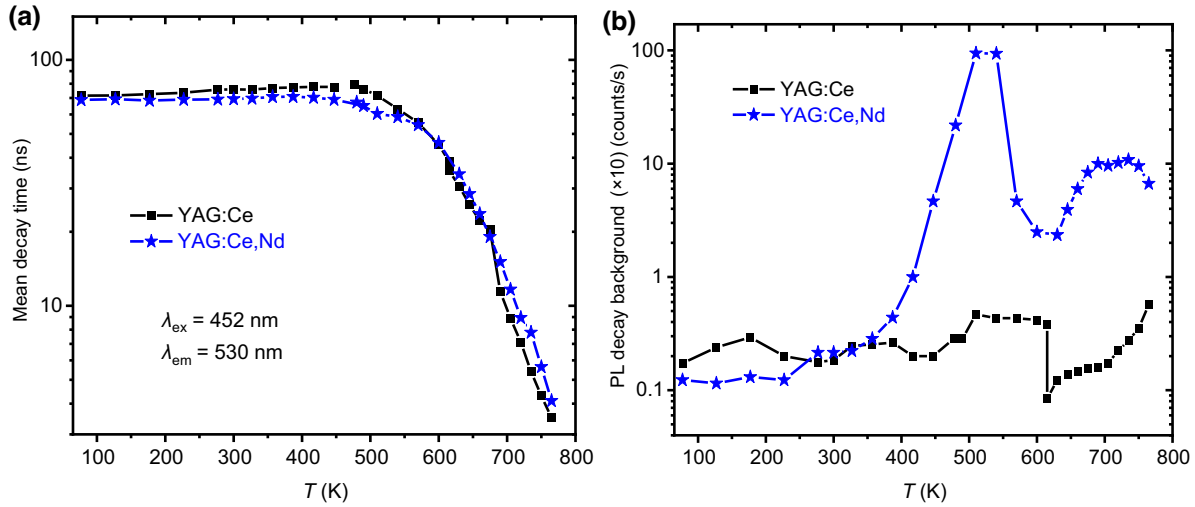

FIG. 12. Temperature dependence of (a) Ce^{3+} photoluminescence-decay times and (b) photoluminescence-decay background intensities in YAG:Ce and YAG:Ce, Nd ceramics, 77–780 K.

excitation sources: a blue LED with an emission wavelength of 455 nm and a laser diode with an emission wavelength of 445 nm. The LED source had a larger spectral width of the photon beam, which contributed to a higher color-rendering-index value. Figures 13(a) and 13(b) show the photoconversion spectra for the LED and LD excitation sources, respectively. The observed differences in the intensity ratio of blue emission and emission from the phosphor may be related to the spectral width of the excitation beam. The photoconversion parameters were calculated from the experimental spectra. The color coordinates (x,y) were plotted on a chromaticity diagram, according to the CIE1931 color space [Fig. 13(c)]. It was shown that codoping with Ln^{3+} and Cr^{3+} strongly influenced the correlated color temperature of the observed emission. Furthermore, the correlated color temperature could also be controlled by the spectral width of the excitation source. The CCT changed between 3400 K (for LD excitation) and 10 000 K (for LED excitation). The photoconversion of the samples with a laser diode exhibited a lower value of the correlated color temperature than that with a LED. This means that excitation with LD produces more neutral white light (CCT 3300–5300 K), while the LED excitation source gives more cold white light (CCT 5300–10 000 K). This is because the excitation bandwidth of the LED is larger than that of the LD, and consequently, contributes more blue light to the photoconversion spectrum. Table II compares the parameters of the color rendering index and luminous efficacy (LE) for ceramics excited with an LD and an LED. In general, better CRI values are obtained under LED excitation due to more homogeneous excitation of the sample. The highest values of CRI are obtained for YAG:Ce^{3+}, Cr^{3+} (73.34) and YAG:Ce^{3+}, Pr^{3+} (71.27) ceramics with LED excitation due to the strongest contribution of the red component to the total emission. Table II shows that the luminous efficacy is higher for ceramics excited with the LED. This is probably due to the wider excitation bandwidth of the LED, which results in a more homogeneous excitation of the ceramics. The best luminous efficacy of 197.66 lm/W is obtained for the nonstoichiometric YAG:Ce, Nd sample. The peculiar structure of the nonstoichiometric sample characterized by the presence of light-scattering centers is principally responsible for its high luminous efficacy. The particle-dispersed system scatters the exciting photon beam more strongly within the volume of the sample. Consequently, a larger number of Ce^{3+} centers can be efficiently excited. This also leads to a more uniform distribution of the exciting photon beam propagating through the sample volume. The absence of light-scattering centers in the highly transparent ceramics

TABLE II. Color-rendering-index parameters of photoconversion of Ce^{3+}-doped and Ln^{3+},Cr^{3+} codoped YAG:Ce^{3+} transparent ceramics.

		YAG:Ce^{3+}	YAG:Ce^{3+}, Er^{3+}	YAG:Ce^{3+}, Ho^{3+}	YAG:Ce^{3+}, Nd^{3+}	YAG:Ce^{3+}, Pr^{3+}	YAG:Ce^{3+}, Cr^{3+}
LED	CRI	60.93	59.61	60.61	66.55	71.27	73.34
LE (lm/W)	144.99	131.75	109.02	197.66	140.55	62.72	
LD	CRI	53.43	50.97	53.56	...	54.98	59.71
LE (lm/W)	121.98	109.95	89.59	114.55	95.77	32.23	

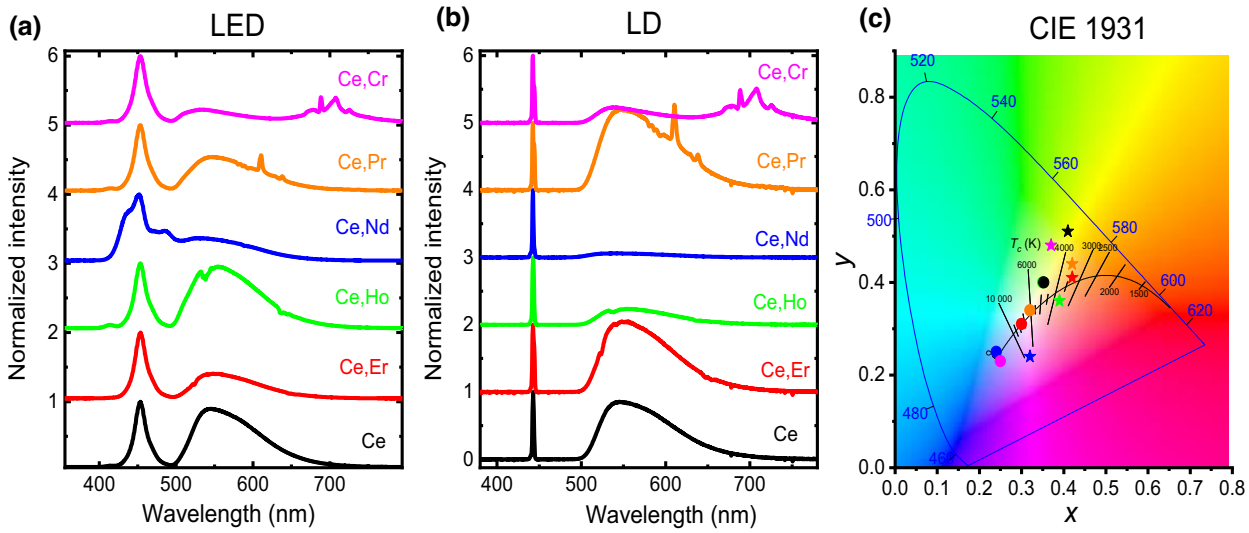

FIG. 13. (a) Photoconversion spectra of Ce^{3+}-doped and Ln^{3+},Cr^{3+} codoped YAG:Ce^{3+} transparent ceramics with broad 455-nm LED excitation and (b) with narrow 445-nm LD excitation; (c) CIE 1931 chromaticity diagram of observed emission for LED (dots) and LD (stars).

(i.e., stoichiometric compositions) leads to the situation that most blue excitation passes through the ceramic without any scattering and only a part of the ceramic sample is effectively excited.

F. Thermoluminescence and afterglow characteristics

Thermally stimulated luminescence measurements were performed to complete the study on the influence of Ln^{3+},Cr^{3+} codopants on the defect structure and charge trapping in YAG:Ce ceramics. The samples were studied under the same conditions, ensuring that the TSL intensities were comparable on an absolute scale. The transparent ceramics were irradiated with 12-eV VUV photons at 300 K. The TSL glow curves were monitored between 300 and 570 K. The TSL glow curve for the undoped YAG host lattice was recorded to identify the formation of charge traps in pure ceramics. The characteristic feature of all TSL glow curves was the presence of a peak at about 320 K exhibiting different intensities. The highest intensity of the TSL signal originated from the pure YAG host lattice, while Ce doping and Ln^{3+},Cr^{3+} codoping significantly reduced the overall TSL intensity. The intensity of the 320-K TSL peaks was especially low in the Ho^{3+} and Cr^{3+} codoped ceramics. In previous studies, this TSL peak was tentatively assigned to a host-related electron trap, which could be an oxygen vacancy ($V_O^{\cdot\cdot}$) [34,52–54]. This assignment could be supported by the PL results, which proved the presence of oxygen vacancies based on the appearance of F^+-center luminescence. Therefore, the intensity of the TSL peak at 320 K should increase in doped samples, but, in fact, it was reduced. The Ce^{4+} ions are more efficient traps for conduction-band electrons than $V_O^{\cdot\cdot}$ or other defects, such as Y_{Al} antisite defects [34,53]. Hence, the electron traps are less populated, resulting in a diminished TSL intensity. This assumption was supported by the TSL glow curve for the YAG:Ce^{3+},Cr^{3+} sample, where the peak centered at 320 K was the least intense. This means that the presence of Cr^{3+} ions provides less-favorable conditions to fill charge traps. Cr^{3+} ions themselves are efficient electron traps, which significantly reduce the population of other electron traps (e.g., $V_O^{\cdot\cdot}$), thus reducing the TSL intensity. The vacuum-referred binding-energy diagram [54] suggests that Ho^{3+} is also a shallow electron trap in the YAG host lattice. Nevertheless, further experimental data are needed to confirm this assumption. The TSL glow peak at 520 K is imposed by Ce^{3+} ions and its intensity is significantly influenced by Ln^{3+},Cr^{3+} codopants. Similarly, previous research [37] revealed the dependence between the intensity of the TSL peak at 520 K and the concentration of Ce^{3+} ions in YAG:Ce single crystals. After air annealing, the TSL intensity was significantly reduced. Therefore, the origin of this TSL peak was assigned to doubly charged oxygen vacancies, $V_O^{\cdot\cdot}$. In conclusion, thermally stimulated luminesce analysis supports the assumption of the presence of stable Ce^{4+} ions and oxygen vacancies in Ce^{3+}-doped and Ln^{3+},Cr^{3+} codoped YAG:Ce^{3+} transparent ceramics, which can arise during the annealing process.

The afterglow decay curves were investigated in Ce^{3+}-doped and Er^{3+}, Ho^{3+}, Pr^{3+}, Nd^{3+}, and Cr^{3+} codoped YAG ceramics after irradiation with 2.75-eV (450-nm) photons for 5 min (Fig. 14). The time-resolved afterglow measurements were performed within a time window ranging from 0 to 600 s. The introduction of Er^{3+}, Ho^{3+}, Pr^{3+}, and Nd^{3+} ions as codopants results in a significant

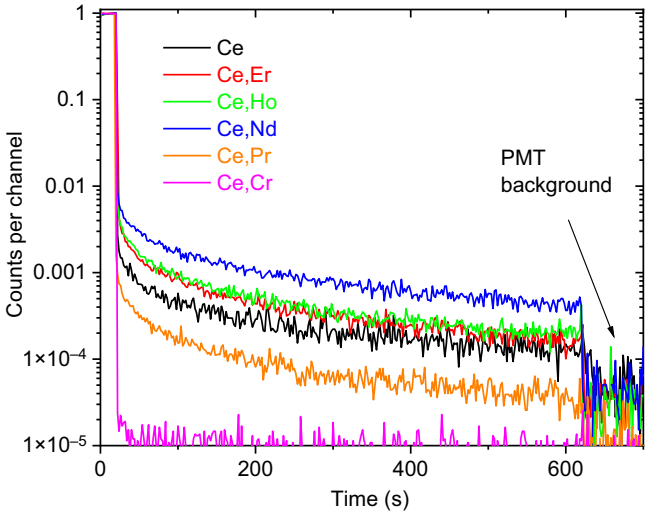

FIG. 14. Afterglow decay curves of Ce^{3+}-doped and Er^{3+}, Ho^{3+}, Pr^{3+}, Nd^{3+}, and Cr^{3+} codoped YAG ceramic compositions after irradiation by 2.75-eV (450-nm) photons for 5 min. PMT, photomultiplier tube.

extension of the overall afterglow duration compared to the Ce^{3+}-doped YAG sample. Particularly, the nonstoichiometric YAG:Ce, Nd sample exhibits the most intense afterglow, approximately 1 order of magnitude higher than that of the reference YAG:Ce sample. Conversely, the nonstoichiometric YAG:Ce, Cr sample displays a negligible afterglow. These findings provide further evidence that codoping with Er^{3+}, Ho^{3+}, Pr^{3+}, and Nd^{3+} increases the concentration of trapping centers in the YAG ceramics lattice. Furthermore, the pronounced afterglow intensity observed in the nonstoichiometric YAG:Ce, Nd sample strongly suggests a higher density of deep trapping centers. These centers possess the ability to effectively store excitation energy and subsequently release it at elevated temperatures, thereby compensating for the decrease in emission intensity associated with the thermal quenching of luminescence [see Fig. 11, Fig. S3c within the Supplemental Material [63], and Fig. 12(b)].

G. Electron paramagnetic resonance analysis

The EPR spectra measured in the YAG:Ce, Ln(Cr) samples are shown in Fig. 15. They are composed of the contributions typical for Ce^{3+}, Er^{3+} (Er^{3+}_{GS} and Er^{3+}_{ES}), Nd^{3+}, and Cr^{3+}. To prove this, the spectra of the YAG:Ce, Cr, YAG:Ce, Er, and YAG:Ce, Nd samples were fitted using

$$\hat{H} = \beta \hat{\mathbf{S}} \hat{\mathbf{g}} \mathbf{H} + \hat{\mathbf{S}} \hat{\mathbf{A}} (\mathrm{Er}^{3+}_{\mathrm{GS}}(\mathrm{Nd}^{3+})) \hat{\mathbf{I}}, \tag{4}$$

$$\hat{H} = \beta g \hat{S}_z H + D(\mathrm{Cr}^{3+}) \left(S_z^2 - \frac{1}{3} S(S+1) \right), \tag{5}$$

where β, $\hat{\mathbf{S}}$, $\hat{S}_z$, $\hat{\mathbf{g}}$, g, $\mathbf{H}$, H, $D(\mathrm{Cr}^{3+})$, $\hat{\mathbf{A}}(\mathrm{Er}^{3+}_{\mathrm{GS}}(\mathrm{Nd}^{3+}))$, and $\hat{\mathbf{I}}$ are the Bohr magneton, vector of the electron-spin operator ($S = 1/2$ for Ce^{3+}, Er^{3+}_{GS}, Er^{3+}_{ES}, and Nd^{3+}) and z component of the electron spin ($S = 3/2$ for Cr^{3+}), the $\mathbf{g}$ tensor (with components g_{1-3}) and g factor, the magnetic field vector and the z component of the magnetic field vector, the zero-field-splitting axial constant of Cr^{3+}, the hyperfine tensor of Er^{3+} and Nd^{3+} (with components A_{1-3}), and the vector of nuclear spin ($I = 7/2$ for ^{167}Er with natural abundance of about 23%, whereas $I = 0$ for the rest of erbium isotopes; $I = 7/2$ for ^{143}Nd and ^{145}Nd with natural abundances of about 12 and 8%, respectively, whereas $I = 0$ for the rest of the neodymium isotopes), respectively. The EPR spectra of Ce^{3+} and Er^{3+}_{ES} were fitted using only the first term in Eq. (4). The EPR spectra of Er^{3+}_{GS} and Nd^{3+} were fitted using Eq. (4). The EPR spectrum of Cr^{3+} was fitted using Eq. (5). The fitting parameters were taken from previously published reports: Ce^{3+} in YAG [55], Er^{3+}_{GS} in YAG [38], Nd^{3+} in YAG [56] and Cr^{3+} in YAG [57]. The $\mathbf{g}$-tensor values determined for Er^{3+}_{ES} were $g_1 = 2.12 \pm 0.01$, $g_2 = 2.03 \pm 0.01$, and $g_3 = 1.99 \pm 0.01$. The values were significantly different from those reported for Er^{3+}_{ES} in Ref. [38] ($g_1 = 1.937$, $g_2 = 1.917$, $g_3 = 1.902$). The Er^{3+}_{ES} signal existed only in the YAG:Ce, Er sample and exhibited a similar temperature dependence to that of Er^{3+}_{GS}. This observation confirmed that Er^{3+}_{ES} was generated by the Er^{3+} ion in its initial excited state [38]. The observed shift in the g factor, in comparison to that reported in Ref. [38], was likely to be due to the inclusion of additional excited states that were permitted by the presence of Ce. Notably, the $g_1 = 1.937$, $g_2 = 1.917$, and $g_3 = 1.902$ $\mathbf{g}$-tensor values were measured for Ce-free YAG:Er [38]. This requires additional investigation and will be published elsewhere.

The computer simulations of EPR spectra were conducted using the software program Easyspin 5.2.35 toolbox [58]. Figure 16 displays both the experimental and calculated spectra.

The spectra obtained from calculations exhibited a high degree of conformity with the spectral locations of Ce^{3+}, Er^{3+} (Er^{3+}_{GS} and Er^{3+}_{ES}), Nd^{3+}, and Cr^{3+} contributions, as depicted in Fig. 16. Therefore, the resonances were appropriately assigned. However, the calculated intensities were different for the larger magnetic field values. The difference is especially well observed in the Cr^{3+} EPR spectrum in Fig. 16(a). This resulted from inhomogeneous broadening of the line as a function of the magnetic field value [59]. The hyperfine structure (HFS) of erbium was not seen very well due to broadening of the resonance lines [Fig. 16(b)] caused by the presence of a relatively large amount of Er^{3+} in the host. In the case of Nd^{3+}, the HFS signals were weak [Fig. 16(c)]. Therefore, to gain better insight into its hyperfine structure, a magnification of the experimental spectrum and its corresponding calculated spectrum are shown in Fig. S6 within the Supplemental

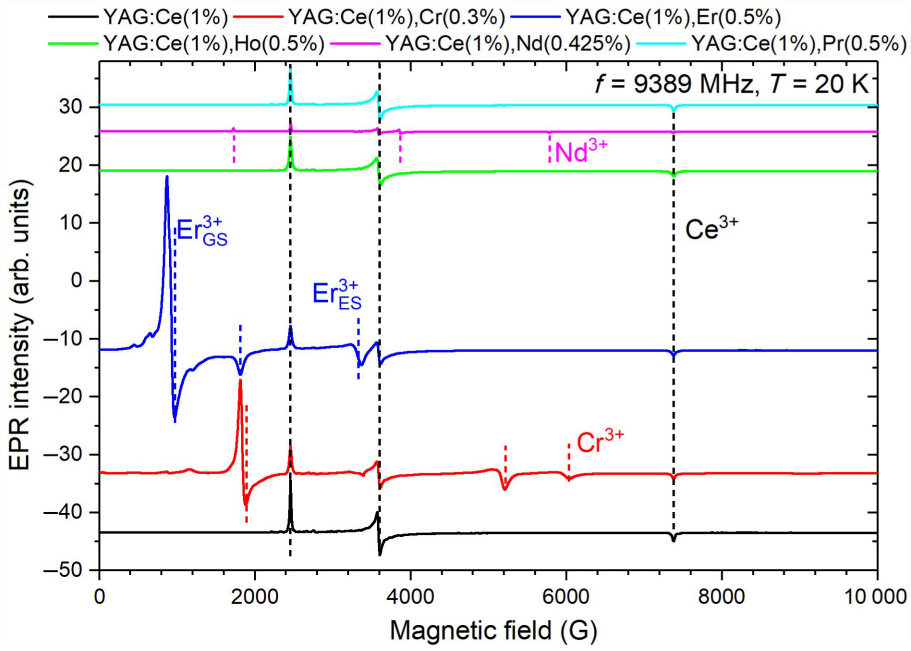

FIG. 15. EPR spectra measured for the YAG:Ce, Ln(Cr) samples. Contributions from Ce^{3+}, Er^{3+} (Er^{3+}_{GS} and Er^{3+}_{ES}, GS and ES mean ground and first excited states, respectively), Nd^{3+}, and Cr^{3+} are indicated by the vertical dashed lines of different colors.

Material [63]. The calculated spectral line positions of the ^{143,145}Nd hyperfine structure were in good agreement with the experimental ones [56]. This provided further evidence that the presence of Nd^{3+} in the YAG host was accurately determined.

The experimental spectra of YAG:Ce, Cr and YAG:Ce, Er are displayed for $T = 20$ K [Figs. 16(a) and 16(b)], whereas the experimental spectrum of YAG:Ce, Nd is displayed for $T = 12$ K [Fig. 16(c)]. In contrast to 20 K, the EPR spectrum in this instance has a peculiar shape (Fig. 15). This shape corresponds well to the integral spectrum, i.e., the absorption spectrum, as opposed to the first derivative, which is the typical continuous-wave EPR spectral shape. Furthermore, the peculiar shape is confined to the region of the Ce^{3+} **g**-tensor values [$g_{Ce1–3}$ in Fig. 16(c)], as described in Ref. [55]. To validate this observation, a new Ce^{3+} spectrum was simulated using Eq. (4) and the parameters provided in Ref. [55] for Ce^{3+}. Notably, there is a resemblance between the unusual shape and the calculated absorption spectrum. This suggests the possible presence of Ce^{3+} in the grain boundaries, where variations in defect occurrence contribute to parameter moderation. Typically, Ce^{3+} is observed at approximately 20 K, and at 12 K the effect of saturation [59] can be anticipated. Consequently, the absorption-like shape of the Ce^{3+} spectrum [Fig. 16(c)] arises due

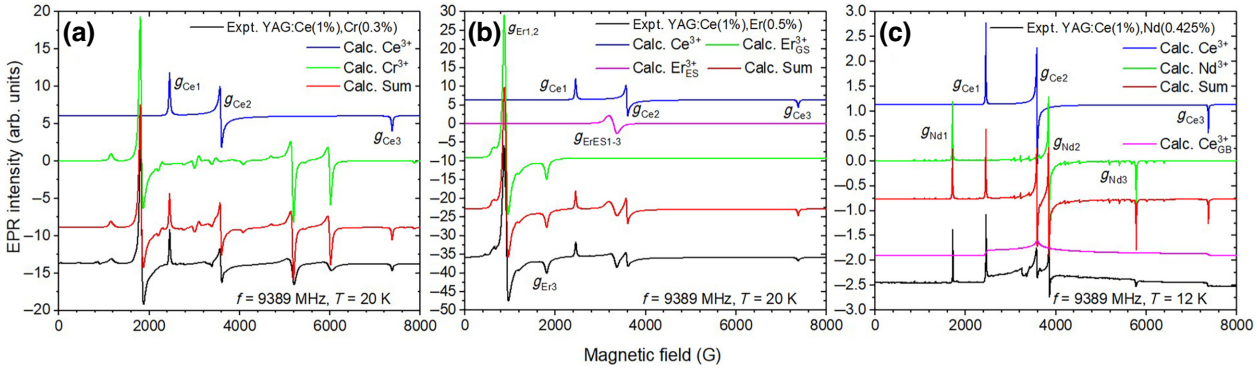

FIG. 16. Experimental and calculated EPR spectra of YAG:Ce, Cr (a), YAG:Ce, Er (b), and YAG:Ce, Nd (c) samples. **g**-tensor values typical for Ce^{3+} [55], Er^{3+} (Er^{3+}_{GS}) [38], and Nd^{3+} [56] are indicated by $g_{Ce1–3}$, $g_{Er1–3}$, and $g_{Nd1–3}$, respectively. Spectral position of Er^{3+}_{ES} is determined and denoted by $g_{ErES1–3}$. Absorption spectrum of Ce^{3+} that arises from the grain boundaries is denoted by Ce^{3+}_{GB}.

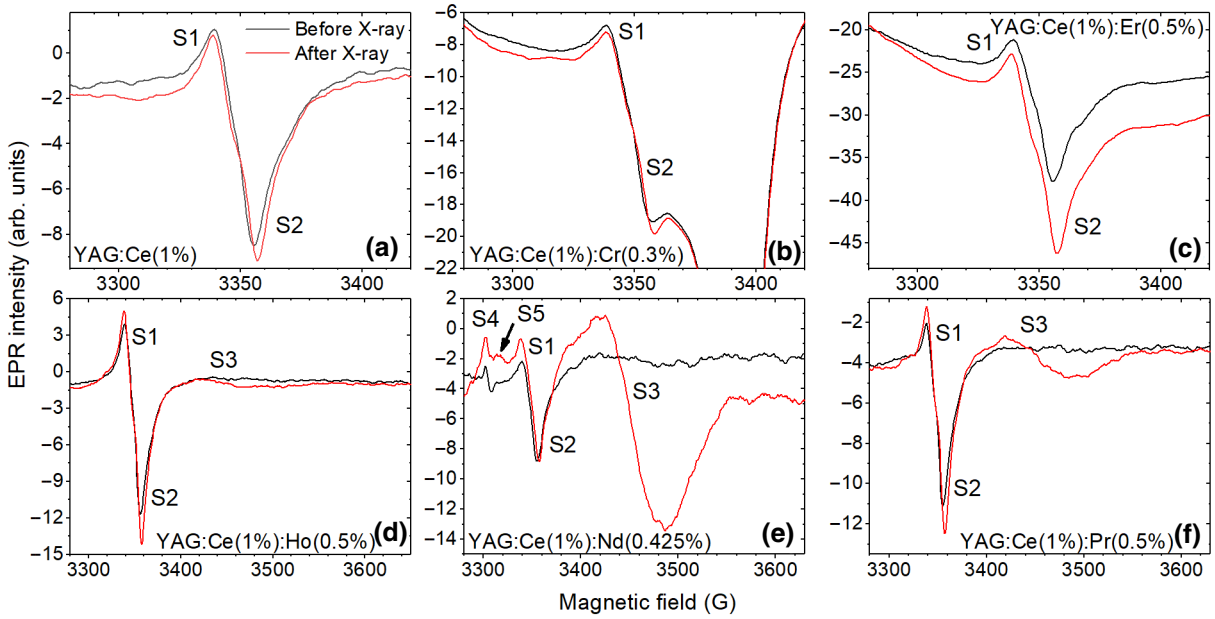

FIG. 17. EPR spectra measured at 70 K before and after x-ray irradiation at room temperature in YAG:Ce (a), YAG:Ce, Cr (b), YAG:Ce, Er (c), YAG:Ce, Ho (d), YAG:Ce, Nd (e), and YAG:Ce, Pr (f) samples. S1,S2 signals exist in the spectra of all the studied samples permanently. S4 signal appears only in YAG:Ce, Nd. S3,S5 signals appear after x-ray irradiation.

to multiple saturated contributions from various cerium centers.

The Ce^{3+} signal was isolated in each of the studied YAG:Ce, Ln(Cr) samples by simulation using Eq. (4) (considering only the first term), as illustrated in Fig. 16. The double-integral intensity of the calculated Ce^{3+} signal was subsequently determined. It is important to note that the double-integral intensity is directly proportional to the number of spins and concentrations of the paramagnetic particle [59]. The resulting double-integral intensities are as follows: nine (YAG:Ce), eight (YAG:Ce, Cr), eight (YAG:Ce, Er), nine (YAG:Ce, Ho), one (YAG:Ce, Nd), and seven (YAG:Ce, Pr).

The total double-integral intensity ratio of the Er^{3+} signal [separated using Eq. (4) considering both Er^{3+}_{GS} and Er^{3+}_{ES}, Fig. 16(b)] to Ce^{3+} in the YAG:Ce, Er sample was found to be 2:1. Considering a doping level of Er^{3+} of 0.5%, it can be inferred that the actual Ce^{3+} content in this sample is at least 0.25% or lower. Consequently, from an intentional Ce^{3+} doping of 1%, at least 0.75% of Ce is expected to appear as Ce^{4+}. By considering the double-integral ratio of Ce^{3+} in all the aforementioned ceramics, the Ce^{4+}:Ce^{3+} ratio can be estimated as follows: 2.6 (YAG:Ce), 3 (YAG:Ce, Cr), 3 (YAG:Ce, Er), 2.7 (YAG:Ce, Ho), 32.3 (YAG:Ce, Nd), and 3.35 (YAG:Ce, Pr). The predominant presence of Ce^{4+} was confirmed by optical absorption measurements, while cerium segregation was not taken into account. The double-integral intensity ratio of Ce^{3+}:Nd^{3+} [using Eqs. (4), (5), and Fig. 16(c)] was estimated to be 2:3.

The EPR spectra of all the ceramics exhibited a prominent signal at a g factor of around 2.00 (S1,S2 in Fig. 17). At room temperature, x-ray irradiation causes a slight increase in these signals, indicating the presence of charge-trapping processes. To determine the origin of the S1,S2 signals, they were fitted with the calculated ones using YAG:Ce, Ho irradiated by x-rays as an example (where signal intensity and spectral resolution were optimal), using the first term in Eq. (4). The calculated and experimental spectra (including components) are depicted in Fig. S7 within the Supplemental Material [63]. $gS1 = 2.007 \pm 0.001$ characterized the S1 signal, whereas $gS2 = 2.001 \pm 0.001$ characterized the S2 signal. According to previous research [60,61], it is likely that both originate from the F^+ center, which is perturbed by a nearby defect. This is consistent with the luminescence study [consider the nonsymmetric shape of the associated emission spectrum, see Fig. 6(a)].

In addition, the other signal at $g = 2.03$ appeared exclusively in YAG:Ce, Nd. Its g factor is typical of centers that trap holes, such as O^- defects [62]. Furthermore, x-ray irradiation generated two additional new signals. The S3 signal at $g = 1.94$ appeared to be very weak in YAG:Ce, Ho [Fig. 17(d)], significantly stronger in YAG:Ce, Pr [Fig. 17(f)], and strongest in YAG:Ce, Nd [Fig. 17(e)]. This correlated with the presence of Ce^{3+}. Note that the least amount of Ce^{3+} was indeed present in the YAG:Ce, Nd sample (cf. Fig. 15 and the preceding discussion). The S3 signal is expected to arise from the perturbed F^+ core, as indicated in previous studies [60,61].

After x-ray irradiation, the S5 signal at $g = 2.02$ appeared only in the YAG:Ce, Nd sample. Again, this is in accordance with the lowest Ce^{3+} content there. It is known that Ce^{3+} acts as a hole trap, producing Ce^{4+}. Therefore, in samples other than YAG:Ce, Nd, it competes with the remaining hole traps and, consequently, with the electron traps, given that a hole trap requires an electron trap to maintain the electroneutrality of a host. Therefore, the lower the Ce^{3+} content (the greater the Ce^{4+}:Ce^{3+} ratio), the greater the number of holes and, consequently, the electron traps (cf. Fig. 17 and the discussion pertaining to the Ce^{4+}:Ce^{3+} ratio).

IV. CONCLUSIONS

Stoichiometric Er, Ho, and Pr codoped YAG:Ce and nonstoichiometric YAG:Ce, Nd and YAG:Ce, Cr transparent ceramics were successfully fabricated using the vacuum reactive sintering technique. The prepared ceramics exhibited a fully densified microstructure according to SEM studies. The Er, Ho, and Pr codoped YAG:Ce ceramics showed a pure garnet phase, while in the nonstoichiometric YAG:Ce, Nd and YAG:Ce, Cr samples, the inclusion of the Al_2O_3 phase was detected, which could contribute as light-scattering centers in ceramics. Doping with Ce^{3+} and codoping in the YAG host caused the formation of specific types of defects, including oxygen vacancies ($V_O^{\cdot\cdot}$) and different nanodefects, which slightly reduced the transparency of ceramics. The EDS mapping and photoluminescence measurements revealed the segregation of Ce^{3+} ions and codopants towards the grain boundary and the formation of Ce^{3+}-Ce^{3+} and Ce^{3+}-Ln^{3+}(Cr^{3+}) pairs. Energy transfer within these pairs was confirmed by photoluminescence spectroscopy results. Temperature-dependent luminescence-intensity measurements for Ce^{3+}-doped and Ce^{3+},Pr^{3+} and Ce^{3+},Cr^{3+} codoped YAG showed that the quenching of Ce^{3+} luminescence started above 400 K, while the nonstoichiometric YAG:Ce, Nd sample showed Ce^{3+} luminescence stability up to 650 K. Photoconversion measurements revealed that better CRI and LE values could be obtained in ceramics under blue LED excitation. The color temperature could also be controlled by the spectral bandwidth of the excitation source. Excitation with LD could produce more neutral white light with CCT values of 3300–5300 K. The photoconversion results demonstrated that suitable light-scattering centers in luminescent ceramics were beneficial for LED and LD lighting devices to achieve higher luminescence efficiency and more homogeneous light generation. The high LE value and high thermal stability of the nonstoichiometric YAG:Ce, Nd ceramic sample demonstrated its potential for further development and optimization of the content of light-scattering (nonstoichiometry) centers to improve its performance. Cerium ions existed mostly as Ce^{4+} in this material. The Ce^{4+}:Ce^{3+} ratio influenced the charge-trapping properties. The existence of two types of F^+ centers was confirmed by EPR as well. The synergistic combination of nonstoichiometry and Nd^{3+}-ion codoping offered a promising path for property tuning in garnet ceramics by manipulating the host stoichiometry. This strategy has scientific significance because it offers the potential for enhanced performance and the discovery of alternative applications of garnet-type materials.

ACKNOWLEDGMENTS

This work was supported by the National Science Centre Poland (NCN) Grant No. 2020/39/D/ST3/02711. Support from the Estonian Research Council (Project No. PUT PRG629) is also gratefully acknowledged. I.R. also acknowledges support from the Polish National Science Centre (Project No. 2018/31/B/ST8/00774).

K.B. conceptualized, wrote, reviewed, and edited the original draft and was responsible for funding acquisition; optical transparency, absorption, PL excitation, and emission spectra measurements and analysis; decay kinetics; TSL measurements and analysis; and analysis of temperature dependence. H.W. prepared the samples and analyzed the microstructure. P.G. prepared and observed raw materials by SEM, analyzed the obtained results, and wrote and edited a draft of the paper. I.R. reviewed and edited the original draft, performed PL excitation and emission spectra measurements and analysis, and analyzed the temperature dependence. M.K. was responsible for the investigation, writing, editing, funding acquisition, and resources. V.N. was responsible for the investigation, reviewing, and editing of the original draft and analyzed the results. A.S. was responsible for the ceramic obtaining technology, ceramic preparation, and analysis of the microstructure. R.T. performed photoconversion and temperature-dependence photoluminescence measurements and analysis. V.J. performed temperature-dependence measurements of decay times. R.K. performed temperature-dependence measurements of decay times. M.W. performed HRTEM measurements and analysis. R.B. was responsible for resources. M.B. performed electron paramagnetic resonance measurements and analysis.

The authors declare that they have no known competing financial interests or personal relationships that could appear to influence the work reported in this paper.

[1] G. Zissis, in *Handbook of Advanced Lighting Technology*, edited by R. Karlicek, C.-C. Sun, G. Zissis, and R. Ma (Springer International Publishing, Cham, 2016), pp. 1–13.

[2] J. Huang, Y. Ni, Y. Ma, Y. Li, Z. Sun, X. Zhu, R. Wang, T. Li, X. Xi, G. Huang, T. Zhou, M. Li, H. Ren, L. Zhang, H. Chen, Composite structure Cr:YAG/Ce:YAG and (Ce, Cr):YAG/Ce:YAG transparent ceramics with high

color rendering index for white LEDs/LDs, Ceram. Int. **47**, 11415 (2021).

[3] Y. Ma, L. Zhang, T. Zhou, B. Sun, Q. Yao, P. Gao, J. Huang, J. Kang, F. A. Selim, C. Wong, H. Chen, and Y. Wang, Weak thermal quenching and tunable luminescence in Ce : $Y_3(Al, Sc)_5O_{12}$ transparent ceramics for high power white LEDs/LDs, Chem. Eng. J. **398**, 125486 (2020).

[4] E. F. Schubert and J. K. Kim, Solid-state light sources getting smart, Science **308**, 1274 (2005).

[5] V. K. Khanna, *Fundamentals of Solid-State Lighting: LEDs, OLEDs, and Their Applications in Illumination and Displays* (CRC Press, Boca Raton, Florida, United States, 2014).

[6] H. Zhao, G. Liu, J. Zhang, J. D. Poplawsky, V. Dierolf, and N. Tansu, Approaches for high internal quantum efficiency green InGaN light-emitting diodes with large overlap quantum wells, Opt. Express **19**, A991 (2011).

[7] M. R. Krames, O. B. Shchekin, R. Mueller-Mach, G. O. Mueller, L. Zhou, G. Harbers, and M. G. Craford, Status and future of high-power light-emitting diodes for solid-state lighting, J. Display Technol. **3**, 160 (2007).

[8] Z. Xia and A. Meijerink, Ce^{3+}-doped garnet phosphors: Composition modification, luminescence properties and applications, Chem. Soc. Rev. **46**, 275 (2017).

[9] D. Han, D. S. Li, G. Li, E. Y. B. Pun, and H. Lin, Efficient radiation releasing in device-level glass ceramics driven by a blue laser, Appl. Opt. **59**, 7012 (2020).

[10] Y. Peng, X. Guo, R. Li, H. Cheng, and M. Chen, Thermally stable WLEDs with excellent luminous properties by screen-printing a patterned phosphor glass layer on a microstructured glass plate, Appl. Opt. **56**, 3270 (2017).

[11] J. Xu, A. Thorseth, C. Xu, A. Krasnoshchoka, M. Rosendal, C. Dam-Hansen, B. Du, Y. Gong, and O. B. Jensen, Investigation of laser-induced luminescence saturation in a single-crystal YAG:Ce phosphor: Towards unique architecture, high saturation threshold, and high-brightness laser-driven white lighting, J. Lumin. **212**, 279 (2019).

[12] K. Bartosiewicz, A. Markovskyi, T. Zorenko, A. Yoshikawa, S. Kurosawa, A. Yamaji, and Y. Zorenko, New efficient scintillating and photoconversion materials based on the self-flux grown $Tb_3Al_5O_{12}$: Ce single crystal, Phys. Status Solidi Rapid Res. Lett. **14**, 2000327 (2020).

[13] Y. Xu, S. Li, P. Zheng, L. Wang, S. You, T. Takeda, N. Hirosaki, and R.-J. Xie, A search for extra-high brightness laser-driven color converters by investigating thermally-induced luminance saturation, J. Mater. Chem. C Mater. Opt. Electron. Devices **7**, 11449 (2019).

[14] J. Kang, L. Zhang, Y. Li, Y. Ma, B. Sun, Y. Liu, T. Zhou, F. A. Selim, C. Wong, and H. Chen, Luminescence declining behaviors in YAG:Ce transparent ceramics for high power laser lighting, J. Mater. Chem. C Mater. Opt. Electron. Devices **7**, 14357 (2019).

[15] A. Markovskyi, W. Gieszczyk, P. Bilski, A. Fedorov, K. Bartosiewicz, K. Paprocki, T. Zorenko, and Y. Zorenko, Composition engineering of $Tb_{3-x}Gd_xAl_{5-y}Ga_yO_{12}$: Ce single crystals and their luminescent, scintillation and photoconversion properties, J. Alloys Compd. **849**, 155808 (2020).

[16] A. Markovskyi, K. Bartosiewicz, W. Chewpraditkul, K. J. Kim, S. Witkiewicz-Lukaszek, T. Zorenko, W. Chewpraditkul, A. Yoshikawa, and Y. Zorenko, Development of novel scintillation and photo-conversion materials based on $Gd_3(Sc, Al, Ga)_5O_{12}$: Ce single crystals grown by micro-pulling-down method, Mater. Sci. Eng. B Solid State Mater. Adv. Technol. **273**, 115395 (2021).

[17] K. Bartosiewicz, V. Babin, K. Kamada, A. Yoshikawa, A. Beitlerova, and M. Nikl, Effects of Gd/Lu ratio on the luminescence properties and garnet phase stability of Ce^{3+} activated $Gd_xLu_{3-x}Al_5O_{12}$ single crystals, Opt. Mater. (Amst.) **80**, 98 (2018).

[18] K. Bartosiewicz, V. Babin, K. Kamada, A. Yoshikawa, J. A. Mares, A. Beitlerova, and M. Nikl, Luminescence quenching and scintillation response in the Ce^{3+} doped $Gd_xY_{3-x}Al_5O_{12}$ ($x = 0.75$, 1, 1.25, 1.5, 1.75, 2) single crystals, Opt. Mater. (Amst.) **63**, 134 (2017).

[19] K. Bartosiewicz, V. Babin, J. A. Mares, A. Beitlerova, Y. Zorenko, A. Iskaliyeva, V. Gorbenko, Z. Bryknar, and M. Nikl, Luminescence and energy transfer processes in Ce^{3+} activated $(Gd, Tb)_3Al_5O_{12}$ single crystalline films, J. Lumin. **188**, 60 (2017).

[20] Y. Tang, S. Zhou, X. Yi, S. Zhang, D. Hao, and X. Shao, The Cr-doping effect on white light emitting properties of Ce:YAG phosphor ceramics, J. Am. Ceram. Soc. **100**, 2590 (2017).

[21] Y. Tang, S. Zhou, X. Yi, D. Hao, X. Shao, and J. Chen, The characterization of Ce/Pr-doped YAG phosphor ceramic for the white LEDs, J. Alloys Compd. **745**, 84 (2018).

[22] B. Wang, J. Ling, Y. Zhou, W. Xu, H. Lin, S. Lu, Z. Qin, and M. Hong, YAG:Ce^{3+}, Mn^{2+} Transparent ceramics prepared by gel-casting for warm white LEDs, J. Lumin. **213**, 421 (2019).

[23] Y. Xie, Y. Yu, J. Gong, C. Yang, P. Zeng, Y. Dong, B. Yang, R. Liang, Q. Ou, and S. Zhang, Encapsulated room-temperature synthesized $CsPbX_3$ perovskite quantum dots with high stability and wide color gamut for display, Opt. Mater. Express **8**, 3494 (2018).

[24] S. Li, Q. Zhu, D. Tang, X. Liu, G. Ouyang, L. Cao, N. Hirosaki, T. Nishimura, Z. Huang, and R.-J. Xie, Al_2O_3–YAG:Ce composite phosphor ceramic: A thermally robust and efficient color converter for solid state laser lighting, J. Mater. Chem. C Mater. Opt. Electron. Devices **4**, 8648 (2016).

[25] B. Xu, Q. Wu, Y. Bao, G. Chen, Y. Wang, and S. Ren, Time-multiplexed stereoscopic display with a quantum dot-polymer scanning backlight, Appl. Opt. **58**, 4526 (2019).

[26] C. Sommer, J. R. Krenn, P. Hartmann, P. Pachler, M. Schweighart, S. Tasch, and F. P. Wenzl, The effect of the phosphor particle sizes on the angular homogeneity of phosphor-converted high-power white LED light sources, IEEE J. Sel. Top. Quantum Electron. **15**, 1181 (2009).

[27] M. H. Nguyen Thi, N. T. Phuong Loan, and H. Van Ngoc, Enhancing light scattering effect of white LEDs with ZnO nanostructures, Int. J. Electr. Comput. Eng. (IJECE) **11**, 3838 (2021).

[28] W. L. Vos, T. W. Tukker, A. P. Mosk, A. Lagendijk, and W. L. IJzerman, Broadband mean free path of Diffuse light in polydisperse ensembles of scatterers for white light-emitting diode lighting, Appl. Opt. **52**, 2602 (2013).

[29] P. Zheng, S. Li, R. Wei, L. Wang, T.-L. Zhou, Y.-R. Xu, T. Takeda, N. Hirosaki, and R.-J. Xie, Unique design strategy for laser-driven color converters enabling superhigh-luminance and high-directionality white light, Laser Photonics Rev. **13**, 1900147 (2019).

[30] C. Milanese, V. Buscaglia, F. Maglia, and U. Anselmi-Tamburini, Disorder and nonstoichiometry in synthetic garnets $A_3B_5O_{12}(A = \mathrm{Y}, \mathrm{Lu}-\mathrm{La}, B = \mathrm{Al}, \mathrm{Fe}, \mathrm{Ga})$. A Simulation Study, Chem. Mater. **16**, 1232 (2004).

[31] J. Nicolas, J. Coutures, J. P. Coutures, and B. Boudot, Sm_2O_3-Ga_2O_3 and Gd_2O_3-Ga_2O_3 phase diagrams, J. Solid State Chem. **52**, 101 (1984).

[32] M. M. Kuklja, Defects in yttrium aluminium perovskite and garnet crystals: Atomistic study, J. Phys. Condens. Matter **12**, 2953 (2000).

[33] K. Bartosiewicz, V. Babin, K. Kamada, A. Yoshikawa, S. Kurosawa, A. Beitlerova, R. Kucerkova, M. Nikl, and Y. Zorenko, Ga for Al substitution effects on the garnet phase stability and luminescence properties of $Gd_3Ga_xAl_{5-x}O_{12}$: Ce single crystals, J. Lumin. **216**, 116724 (2019).

[34] K. Bartosiewicz, A. Markovskyi, T. Horiai, D. Szymański, S. Kurosawa, A. Yamaji, A. Yoshikawa, and Y. Zorenko, A study of Mg^{2+} ions effect on atoms segregation, defects formation, luminescence and scintillation properties in Ce^{3+} doped $Gd_3Al_2Ga_3O_{12}$ single crystals, J. Alloys Compd. **905**, 164154 (2022).

[35] M. A. Chaika, P. Dluzewski, K. Morawiec, A. Szczepanska, K. Jablonska, G. Mancardi, R. Tomala, D. Hreniak, W. Strek, N. A. Safronova, A. G. Doroshenko, S. V. Parkhomenko, and O. M. Vovk, The role of Ca^{2+} ions in the formation of high optical quality Cr^{4+}, Ca:YAG ceramics, J. Eur. Ceram. Soc. **39**, 3344 (2019).

[36] A. K. Bedyal, V. Kumar, R. Prakash, O. M. Ntwaeaborwa, and H. C. Swart, A near-UV-converted $LiMgBO_3 : Dy^{3+}$ nanophosphor: Surface and spectral investigations, Appl. Surf. Sci. **329**, 40 (2015).

[37] C. Varney and F. Selim, Positron lifetime measurements of vacancy defects in complex oxides, Acta Phys. Pol., A **125**, 764 (2014).

[38] M. Buryi, A. M. Gaston-Bellegarde, J. Pejchal, F. Levchenko, Z. Remeš, K. Ridzoňová, V. Babin, and S. Chertopalov, The role of Er^{3+} content in the luminescence properties of $Y_3Al_5O_{12}$ single crystals: Incorporation into the lattice and defect state creation, Crystals (Basel) **13**, 562 (2023).

[39] R. D. Shannon, Revised effective ionic radii and systematic studies of interatomic distances in halides and chalcogenides, Acta Crystallogr. A **32**, 751 (1976).

[40] L. Jia, J. Zhu, Y. Boyaryntseva, I. Gerasymov, B. Grynyov, and O. Sidletskiy, Effect of carbon doping on F-type defects in YAG and YAG:Ce crystals, Phys. Status Solidi B Basic Res. **258**, 2100325 (2021).

[41] M. Springis, A. Pujats, and J. Valbis, Polarization of luminescence of colour centres in YAG crystals, J. Phys. Condens. Matter **3**, 5457 (1991).

[42] E. Zych, C. Brecher, A. J. Wojtowicz, and H. Lingertat, Luminescence properties of Ce-activated YAG optical ceramic scintillator materials, J. Lumin. **75**, 193 (1997).

[43] V. Bachmann, C. Ronda, and A. Meijerink, Temperature quenching of yellow Ce^{3+} luminescence in YAG:Ce, Chem. Mater. **21**, 2077 (2009).

[44] W. Zhao, S. Anghel, C. Mancini, D. Amans, G. Boulon, T. Epicier, Y. Shi, X. Q. Feng, Y.B. Pan, V. Chani, and A. Yoshikawa, Ce^{3+} dopant segregation in $Y_3Al_5O_{12}$ optical ceramics, Opt. Mater. (Amst.) **33**, 684 (2011).

[45] N. C. George, A. J. Pell, G. Dantelle, K. Page, A. Llobet, M. Balasubramanian, G. Pintacuda, B. F. Chmelka, and R. Seshadri, Local environments of dilute activator ions in the solid-state lighting phosphor $Y_{3-x}Ce_xAl_5O_{12}$, Chem. Mater. **25**, 3979 (2013).

[46] P. Głuchowski, R. Pązik, D. Hreniak, and W. Stręk, Luminescence properties of Cr^{3+}:$Y_3Al_5O_{12}$ nanocrystals, J. Lumin. **129**, 548 (2009).

[47] R. Guan, L. Cao, Y. You, and Y. Cao, The luminescence properties and energy transfer from Ce^{3+} to Pr^{3+} for YAG:Ce^{3+} Pr^{3+} phosphors, J. Nanomater. **2015**, 1 (2015).

[48] R. Ma, C. Ma, J. Zhang, J. Long, Z. Wen, X. Yuan, and Y. Cao, Energy transfer properties and enhanced color rendering index of chromaticity tunable green-yellow-red-emitting $Y_3Al_5O_{12} : Ce^{3+}, Cr^{3+}$ phosphors for white light-emitting diodes, Opt. Mater. Express **7**, 454 (2017).

[49] S. Hu, C. Lu, X. Liu, and Z. Xu, Optical temperature sensing based on the luminescence from YAG:Pr transparent ceramics, Opt. Mater. (Amst.) **60**, 394 (2016).

[50] S. P. Feofilov, A. B. Kulinkin, T. Gacoin, G. Mialon, G. Dantelle, R. S. Meltzer, and C. Dujardin, Mechanisms for Ce^{3+} excitation at energies below the zero-phonon line in YAG crystals and nanocrystals, J. Lumin. **132**, 3082 (2012).

[51] S. Stojadinović and A. Ćirić, Ce^{3+}/Eu^{2+} doped Al_2O_3 coatings formed by plasma electrolytic oxidation of aluminum: Photoluminescence enhancement by $Ce^{3+} \rightarrow Eu^{2+}$ energy transfer, Coatings **9**, 819 (2019).

[52] J.-P. Zhong, H.-B. Liang, Q. Su, J.-Y. Zhou, and J.-Y. Wang, Spectroscopic properties of vacancies and trap levels in $Lu_3Al_5O_{12} : Ce^{3+}$ crystals, Trans. Nonferrous Met. Soc. China **19**, 1628 (2009).

[53] S. Liu, X. Feng, Z. Zhou, M. Nikl, Y. Shi, and Y. Pan, Effect of Mg^{2+} codoping on the scintillation performance of LuAG : Ce ceramics: Effect of Mg^{2+} codoping on the scintillation performance of LuAG : Ce ceramics, Phys. Status Solidi Rapid Res. Lett. **8**, 105 (2014).

[54] P. Dorenbos, A review on how lanthanide impurity levels change with chemistry and structure of inorganic compounds, ECS J. Solid State Sci. Technol. **2**, R3001 (2013).

[55] V. Laguta, M. Buryi, V. Babin, P. Machek, S. Zazubovich, K. Bartosiewicz, S. Kurosawa, A. Yamaji, A. Yoshikawa de, K. Uličná, V. Chlan, H. Štěpánková and M. Nikl, Ce^{+} incorporation and defect-creation processes imposed by x-ray and UV irradiation in Li-codoped $Y_3Al_5O_{12}$: Ce scintillation crystals, J. Mater. Chem. C Mater. Opt. Electron. Devices **11**, 1346 (2023).

[56] P. Nikolova and B. L. Timan, EPR investigation of the structural perfection of Nd^{3+} doped YAG single crystals, J. Appl. Spectrosc. **36**, 348 (1982).

[57] M. Buryi, L. Havlák, V. Jarý, J. Bárta, V. Laguta, A. Beitlerová, J. Li, X. Chen, Y. Yuan, Q. Liu, Y. Pan and

M. Nikl, Specific absorption in $Y_3Al_5O_{12}$: Eu ceramics and the role of stable Eu^{2+} in energy transfer processes, J. Mater. Chem. C Mater. Opt. Electron. Devices **8**, 8823 (2020).

[58] S. Stoll and A. Schweiger, EasySpin, a comprehensive software package for spectral simulation and analysis in EPR, J. Magn. Reson. **178**, 42 (2006).

[59] A. Abragam and B. Bleaney, *Electron Paramagnetic Resonance of Transition Ions* (Oxford University Press, Cary, NC, 2012).

[60] W. E. Hagston, Implications of the theory for defect centres having *g* factors close to the free spin values, J. Phys. **3**, 1233 (1970).

[61] A. Watterich, R. H. Bartram, O. R. Gilliam, L. A. Kappers, G. J. Edwards, I. Földvári, and R. Voszka, ESR identification of radiation-induced oxygen vacancy centers in paratellurite, Phys. Rev. B Condens. Matter **32**, 2533 (1985).

[62] M. Buryi, V. Babin, V. Laguta, D. A. Spassky, V. Nagirnyi, and V. N. Shlegel, Electron and hole trapping in Li_2MoO_4 cryogenic scintillator, Opt. Mater. (Amst.) **114**, 110971 (2021).

[63] See the Supplemental Material at http://link.aps.org/supplemental/10.1103/PhysRevApplied.20.014047 for additional data and discussion, including Figures S1–S7 and Table S1.

Correction: The omission of an institutional name in the last affiliation in the front matter has been corrected.